



# Aerodynamic performance and wake development of airfoils with wavy leading edges

Weijie Chen <sup>a,\*</sup>, Weiyang Qiao <sup>a,b</sup>, Zuojun Wei <sup>c</sup>

<sup>a</sup> School of Power and Energy, Northwestern Polytechnical University, Xi'an, Shaanxi, China

<sup>b</sup> Key Laboratory of Aerodynamic Noise Control, China Aerodynamics Research and Development Centre, Mianyang, Sichuan, China

<sup>c</sup> Department of Mechanics and Aerospace Engineering, Southern University of Science and Technology, Shenzhen, Guangdong, China

## ARTICLE INFO

### Article history:

Received 8 July 2020

Received in revised form 30 August 2020

Accepted 14 September 2020

Available online 19 September 2020

Communicated by Qiulin Qu

### Keywords:

Wavy leading edge

Scale-adaptive simulation

Aerodynamic performance

Wake development

## ABSTRACT

A comprehensive numerical investigation is performed to study the aerodynamic performance and wake development of a NACA0012 airfoil with wavy leading edges (WLE). The WLEs are in the form of sinusoidal profiles with two design parameters of amplitude and wavelength. Parametric studies of the amplitude and wavelength are conducted to better understand the effect of WLEs. The chord length based Reynolds number is 400 000 and the angle of attack varies from 0° to 20°. For angles of attack less than the stall angle, steady Reynolds-averaged Navier-Stokes (RANS) computations are carried out using the SST (Shear Stress Transportation)  $k-\omega$  turbulence model. For the post-stall angles of attack, unsteady simulations are carried out using the SST-SAS (Scale-Adaptive Simulation) model to solve the transient separation flow. The numerical results indicate that the aerodynamic performance of the wavy airfoil is sensitive to both the amplitude and wavelength of the WLEs. The WLE with a larger amplitude and smaller wavelength results in a worse aerodynamic performance. The drag coefficient is decreased significantly by the WLEs in the post-stall region. In addition, the wavy airfoils possess a soft stall process without the abrupt loss of the lift when the amplitude is large enough. The wake profiles for the wavy airfoils differ significantly from those for a conventional airfoil, especially for high angles of attack. In the post-stall regime of the baseline airfoil, the wavy airfoils have a higher wake deficit compared to the baseline airfoil, but the turbulence kinetic energy is reduced significantly. The leading edge separation vortex generated by the baseline airfoil is broken down into small vortices by the wavy modification, leading to a reduced lift and drag fluctuations.

© 2020 Elsevier Masson SAS. All rights reserved.

## 1. Introduction

Flow control devices are commonly used on airfoils, wings and blades to improve their aerodynamic performance [1–4]. An intriguing passive flow control model has been inspired by the undulating tubercles observed on the leading edges of the pectoral flippers of the humpback whale. Despite its large size, the humpback whale is able to perform complex underwater maneuvers to catch the prey. Fish and Battle [5] were the first to postulate that the wavy leading edges contribute to the extraordinary maneuverability of the humpback whale by maintaining lift at high angles of attack. Since then, the WLE has become the subject of several

experimental [6–23], numerical [24–30] and theoretical [31,32] studies to explore its benefits on the aerodynamic performance of airfoils and wings.

Miklosovic et al. investigated the effect of the WLE on wing aerodynamic performance through wind tunnel measurements [6]. It was found that the addition of leading edge tubercles to a scale model of an idealized humpback whale flipper can delay the stall angle by approximately 40%, while increasing lift and decreasing drag. However, they further pointed out that the effects were vastly different between the infinite (full-span) and finite (semi-span) wings [7]. For the full-span airfoil, the lift was 38% lower and the drag 137% higher as a result of the WLE before stall for the baseline airfoil. Above the stall point of the baseline airfoil, the WLE increased lift by 48% and decreased drag by about 6%. The aerodynamic characteristics of airfoils with leading edge sinusoidal tubercles were measured in a water tunnel by Johari et al. [8]. It was observed that the amplitude of the WLE had distinct effects on the performances of the airfoils, whereas the wavelength had negligible effects. Wind-tunnel measurements were conducted by

\* Corresponding author.

E-mail address: [cwj@mail.nwpu.edu.cn](mailto:cwj@mail.nwpu.edu.cn) (W. Chen).

## Nomenclature

$A$	.....	Amplitude
$C$	.....	Chord length
$C_L$	.....	Lift coefficient
$C_D$	.....	Drag coefficient
$C_f$	.....	Wall shear stress coefficient
$C_p$	.....	Pressure coefficient
$p$	.....	Static pressure
$Q$	....	Second invariant property of the velocity gradient
$U_0$	.....	Free-stream velocity
$W$	.....	Wavelength
$x, y, z$	.....	Cartesian coordinates
$y^+$	.....	Normalized wall-normal coordinate
$\delta$	.....	Dirac delta function
$\Delta t$	.....	Normalized time step

$\rho$	.....	Density
$\nu$	.....	Kinematic viscosity
$\tau_x$	.....	Streamwise mean wall shear stress
<b>Abbreviations</b>		
AOA	.....	Angle of attack
CFD	.....	Computational fluid dynamics
DES	.....	Detached eddy simulation
LES	.....	Large eddy simulation
RANS	.....	Reynolds-averaged Navier-Stokes
SAS	.....	Scale-adaptive simulation
SST	.....	Shear stress transportation
TKE	.....	Turbulence kinetic energy
WLE	.....	Wavy leading edge

Guerreiro and Sousa to study the application of sinusoidal leading edges to the design of micro air vehicles [10]. The experiments indicated that both the amplitude and wavelength of the WLEs play important roles in the aerodynamic force. Force measurements were conducted by Bolzon et al. on wavy swept NACA0021 wings [12,15]. The experimental results showed that between 0 and 8° angles of attack, the lift was reduced by 4–6% by the tubercles, while the drag was reduced by 7–9.5%. At angles of attack larger than 8°, tubercles typically decreased the lift and increased the drag. Wei et al. systematically investigated the effect of leading-edge tubercles on the hydrodynamic/aerodynamic performance of infinite-wings, finite-wings, and tapered swept-back wings, using both water tunnel and wind tunnel facilities [18–23]. Their experimental studies confirmed that the tubercles act as vortex generators. A pair of counter-rotating vortex is produced by each tubercle and the induced vortices play an essential role on the downstream flow structures [14,17,18].

A RANS simulation was applied by Weber et al. to study the performance of an idealized humpback whale flipper with leading edge protuberances [24]. It was found that the tubercle flipper still possessed significant regions of attached flow at high angles of attack, which contributes to its ability of maintain increased lift in the post-stall regime. A detached-eddy simulation (DES) was conducted by Malipeddi et al. to study the effects of leading edge protuberances on the aerodynamic performance of a NACA2412 airfoil [26]. It was also observed that the amplitude of the tubercles significantly affects the airfoil performance, while the wavelength has little effect. A large-eddy simulation (LES) was performed by Skillen et al. to investigate the flow over an airfoil with leading-edge undulations [28]. It was observed that the WLE geometry produces a spanwise pressure gradient that drives a secondary flow toward the trough region, while it enhances the momentum exchange in the boundary layer behind the peak, leading to a delayed stall.

Nierop et al. developed an aerodynamic model based on the lifting-line theory to explain the improved performance by the leading edge tubercles [31]. The theoretical analysis indicated that as the amplitude of the tubercles is increased, the lift curve flattens out, while the stall delay is insensitive to the wavelength of the tubercles. Nonlinear lifting-line theory was employed by Rostamzadeh et al. to study the effect of wavy surfaces on the NACA0021 airfoil performance [32]. The results showed that the wavy surface generally degrades the performance in the pre-stall regime, while improves the performance in the post-stall regime. In addition to the aerodynamic aspects, WLEs have also been employed to reduce the airfoil trailing edge noise [33–35] and airfoil-turbulence interaction noise [36–38]. The noise reduction effects of

WLEs are not further discussed here since the focus of the present study is on the aerodynamic performance. A detailed review on noise reduction by WLEs can be found in previous studies of the present author [39–41].

The aforementioned discussions indicate that the WLE geometry is a potential passive control modification to improve the airfoil performance. However, the effects of the WLE geometry depend on the planform shape, the airfoil section, the angle of attack and the Reynolds number. The influences of the tubercle amplitude and wavelength still have no consensus. Furthermore, to the best knowledge of the present authors, the effect of wavy modification on wake development has not been well studied previously. In this paper, numerical simulations are employed to compute the turbulent flow around the wavy airfoils. Parametric studies of the amplitude and wavelength characteristics are performed. The force coefficients, the instantaneous flow patterns and the wake characteristics are compared with a conventional NACA0012 airfoil.

## 2. Airfoil models

As shown in Fig. 1(a), the leading edge line of the wavy airfoil is in the form of a sinusoidal profile. The averaged leading edge line coincides with that of the baseline NACA0012 airfoil such that the mean chord and the wetted area are maintained constant. The design parameters of a wavy airfoil are the amplitude ( $A$ ) and wavelength ( $W$ ).

The chord of the wavy airfoil versus the spanwise coordinate is of the form

$$c(z) = c + \frac{A}{2} \cos\left(\frac{2\pi}{W}z\right) \quad (1)$$

The coordinates of the baseline airfoil are modified in the nose region according to Eq. (2).

$$\begin{cases} x_{new} = \begin{cases} \frac{x_{old}}{x_{max}} [x_{max} + (c(z) - c)] - [c(z) - c], & x_{old} < x_{max} \\ x_{old}, & x_{old} \geq x_{max} \end{cases} \\ y_{new} = y_{old}, \end{cases} \quad (2)$$

where subscripts *old* and *new* refer to the baseline and modified airfoils, respectively. Subscript *max* represents to the location of the maximum thickness, as shown in Fig. 1(b). The  $x$  coordinates near the nose are stretched or contracted in line with the spanwise chord of the wavy airfoil, while the rear coordinates are unchanged.

Several previous studies on the aerodynamic effects of the WLE modification are summarized in Table 1. The airfoil sections, the

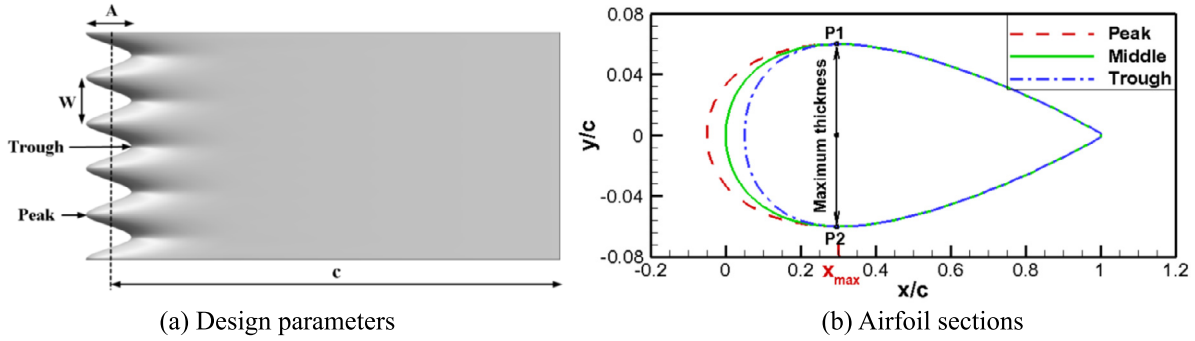


Fig. 1. Sketch of the airfoil with wavy leading edges.

**Table 1**

Previous studies on the aerodynamic effect of the WLE geometry.

Year	Authors	Airfoil section	Method	$A/c$	$W/c$	Re	AOA ( $^{\circ}$ )
2007	Miklosovic et al. [7]	NACA0020	Exp.	0.04	0.42	631000	0–25
2007	Johari et al. [8]	NACA634-021	Exp.	0.05–0.24	0.25–0.50	183000	–6–30
2011	Hansen et al. [9]	NACA0021/NACA65021	Exp.	0.03–0.11	0.11–0.86	120000	–5–25
2011	Yoon et al. [25]	NACA0020	RANS	0.025	0.20	1000000	0–40
2012	Guerreiro et al. [10]	NASALS(1)0417	Exp.	0.06–0.12	0.25–0.50	140000	0–30
2012	Malipeddi et al. [26]	NACA2412	DES	0.025–0.05	0.25–0.50	570000	0–20
2013	Zhang et al. [11]	NACA634-021	Exp.	0.12	0.25	50000	0–90
2013	Lin et al. [27]	NACA0012	LES	0.12	0.24	160000	0–20
2015	Wei et al. [18]	NACA634-021	Exp.	0.05–0.24	0.25–0.50	14000	0–20
2015	Skillen et al. [28]	NACA0021	LES	0.03	0.11	120000	20
2016	Keerthi et al. [13]	NACA65209	Exp.	0.03–0.07	0.125–0.17	130000	0
2016	Hansen et al. [14]	NACA0021	Exp./URANS	0.11	0.43	2230	5, 10
2017	Sudhakar et al. [16]	S1223	Exp.	0.025	0.25	270000	–4–26
2017	Torro et al. [29]	NACA0021	LES	0.03	0.11	120000	20
2018	Wei et al. [20]	SD7032	Exp.	0.24	0.47	220000	–7–29
2019	Wei et al. [23]	NACA634-021	Exp.	0.05–0.24	0.25–0.50	180000	–6–26
–	Present study	NACA0012	RANS/SAS	0.025–0.10	0.10–0.40	400000	0–20

**Table 2**

Design parameters of the present WLE geometries.

Airfoil	$A$ (mm)	$W$ (mm)	$A/c$ (%)	$W/c$ (%)	$A/W$
Baseline	–	–	–	–	–
A2.5W10	3.75	15	2.5	10	0.25
A5W10	7.5	15	5	10	0.5
A10W10	15	15	10	10	1.0
A10W20	15	30	10	20	0.5
A10W40	15	60	10	40	0.25

investigation methods, the range of tubercle amplitude and wavelength, the Reynolds number and the range of the angles of attack are summed up in this table. It can be seen that various airfoil sections, wavy design parameters and flow conditions have been studied. In the present study, a NACA0012 airfoil with a chord of 150 mm is chosen as the baseline case for comparison. Three amplitudes of  $0.025c$ ,  $0.05c$  and  $0.1c$  are chosen with three wavelengths of  $0.1c$ ,  $0.2c$  and  $0.4c$ . The chosen amplitudes and wavelengths in this study fall within the range of values associated with the humpback whale flippers [5]. The design parameters of the five WLE geometries used in this study are listed in Table 2. The wavy airfoils are labeled by the combinations of the non-dimensional percentage of the amplitude and wavelength.

### 3. Numerical methodology

#### 3.1. Governing equations

The commercial CFD package ANSYS-CFX is employed for all the numerical simulations [42]. The governing equations are the following Reynolds-averaged Navier–Stokes equations

$$\frac{\partial \bar{u}_i}{\partial x_i} = 0 \quad (3)$$

$$\frac{\partial \bar{u}_i}{\partial t} + \frac{\partial}{\partial x_j} (\bar{u}_i \bar{u}_j) = -\frac{1}{\rho} \frac{\partial \bar{p}}{\partial x_i} + \frac{\partial}{\partial x_j} \left[ \nu \left( \frac{\partial \bar{u}_i}{\partial x_j} + \frac{\partial \bar{u}_j}{\partial x_i} - \frac{2}{3} \delta_{ij} \frac{\partial \bar{u}_k}{\partial x_k} \right) \right] + \frac{\partial}{\partial x_j} \left( -\bar{u}'_i \bar{u}'_j \right) \quad (4)$$

where  $x_i$  are the Cartesian coordinates,  $u_i$  are the corresponding velocity components,  $\rho$  is the density,  $p$  is the pressure,  $\nu$  is the kinematic viscosity,  $\delta$  is the Dirac delta function and the overbar represents the ensemble average.

For angles of attack less than the stall angle, the Reynolds stress term is closed by using the SST  $k-\omega$  model [43]. The  $k-\omega$  based SST model accounts for the transport of the turbulent shear stress and gives highly accurate predictions of the onset and the amount of flow separation under adverse pressure gradients. The SST  $k-\omega$  model is more accurate and reliable for a wider class of flows than the standard  $k-\omega$  model. When the angle of attack is greater than the stall angle, the flow field is solved by using the unsteady SST-SAS model [44,45]. The SAS model is an improved URANS formulation, which is based on the introduction of the von Karman length-scale into the turbulence scale equation. The information provided by the Karman length-scale allows the SAS model to dynamically adjust to resolved structures in a URANS simulation, which results in a LES-like behavior in unsteady regions of the flow field. It has been demonstrated that the SAS model is suitable for a wide range of complex engineering applications and it systematically leads to improved results compared to RANS or classical URANS simulations [46–50].

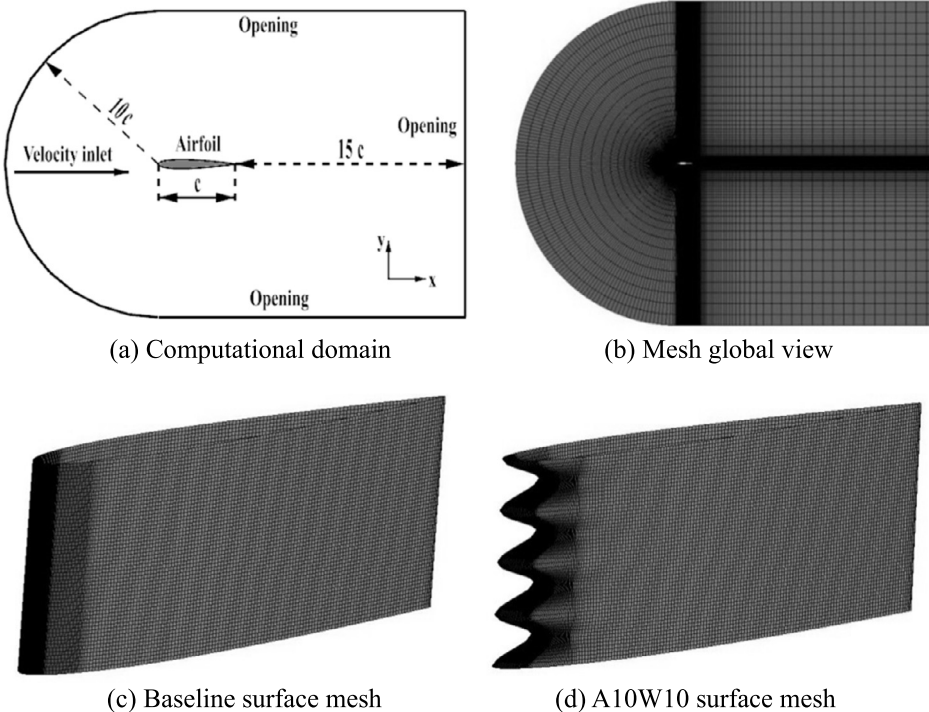


**Fig. 2.** Illustration of the computational domain and mesh.

### 3.2. Computational domain and mesh

As shown in Fig. 2(a), the computational domain extends  $26c$  ( $c = 150$  mm is the chord) in the streamwise direction,  $20c$  in the cross-stream direction and  $0.4c$  in the spanwise direction. The meshes are refined around the airfoil and in the wake region and stretched to the far-field, as shown in Fig. 2(b). The surface meshes on the baseline and A10W10 airfoils are depicted in Fig. 2(c) and (d), respectively. There are 490 grid nodes around the airfoil in the circumferential direction. The first mesh size normal to the wall surface in turbulent units is  $y^+ \leq 10$ . The mesh is composed of 3.25 million grid nodes with 57 nodes along the span. The total grid nodes are almost consistent for the baseline and wavy airfoils. The mesh independence study and validation are conducted in the following section.

The incoming freestream velocity is 40 m/s and the chord based Reynolds number is 400 000. An adiabatic no-slip condition is imposed on the solid airfoils and the periodic boundary condition is imposed in the spanwise direction. The angle of attack varies from 0 to  $20^\circ$  with an interval of  $1^\circ$ . Steady simulations with the SST  $k-\omega$  turbulence model are carried out in the pre-stall region, while unsteady simulations with the SST-SAS model are performed in the post-stall regime. The computation time step for the unsteady simulation is  $5 \times 10^{-5}$  s and the corresponding characteristic time step is  $\Delta t = 0.013c/U_0$ . The advection terms and turbulence numeric terms are discretized using a high resolution scheme. A second order backward Euler scheme is employed for the time marching.

### 3.3. Mesh independence study and validation

The lift coefficient and drag coefficient of an airfoil are defined by

$$C_L = \frac{F_L}{0.5\rho U_0^2 S} \quad (5)$$

$$C_D = \frac{F_D}{0.5\rho U_0^2 S} \quad (6)$$

**Table 3**  
Mesh independence study of the A10W10 airfoil.

A10W10	Total nodes, million	$C_L$	$C_D$	$\Delta C_L (\%)$	$\Delta C_D (\%)$
Mesh 1	1.88	0.4710	0.0205	-1.69	4.59
Mesh 2	2.34	0.4749	0.0200	-0.88	2.04
Mesh 3	2.80	0.4774	0.0198	-0.36	1.02
Mesh 4	3.25	0.4791	0.0196	-	-
Mesh 5	3.71	0.4803	0.0195	0.25	-0.51

where  $F_L$  and  $F_D$  are the lift and drag, respectively,  $S$  is the projected area of the airfoil. A mesh independence study is conducted for the A10W10 airfoil with five mesh sizes of 1.88, 2.34, 2.80, 3.25 and 3.71 million nodes. The A10W10 airfoil is first chosen for mesh independence study because it has the largest amplitude and smallest wavelength, which is the most difficult airfoil to satisfy the grid convergence. The calculated aerodynamic characteristics of the A10W10 airfoil at an angle of attack of  $5^\circ$  are summarized in Table 3 for the five mesh cases. The relative variations of the lift and drag coefficients are based on the results of Mesh 4. It is observed that the relative differences for the Mesh 1 (1.88 M) case are  $-1.69\%$  and  $4.59\%$ , respectively. When the grid nodes are increased to 3.71 M, the relative differences are within 1%.

The pressure coefficient is defined by

$$C_p = \frac{p - p_0}{0.5\rho U_0^2} \quad (7)$$

where  $p$  is the static pressure on the airfoil surface,  $p_0$  is the ambient pressure. The pressure coefficients at the peak and trough positions of the A10W10 airfoil are plotted in Fig. 3. It can be seen that the pressure distributions obtained by the five meshes exhibit consistent results. Fig. 4 shows the mean streamwise velocity and turbulence kinetic energy (TKE) distributions in the wake region of the A10W10 airfoil corresponding to the peak position. The results in the trough position show similar feature and are not shown for clarity. The wake profiles are plotted at various downstream locations of  $x/c = 1.1, 1.2, 1.3, 1.5$  and  $2.0$  relative to the leading edge of the airfoil. It can be seen that the results tend to be conver-

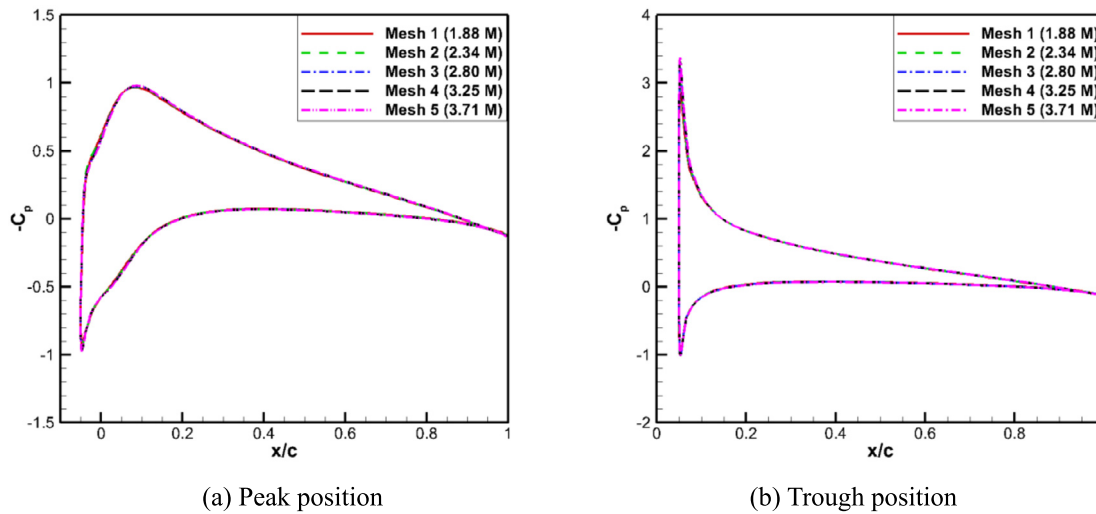


**Fig. 3.** Mesh independence study on the surface pressure distribution of the A10W10 airfoil.

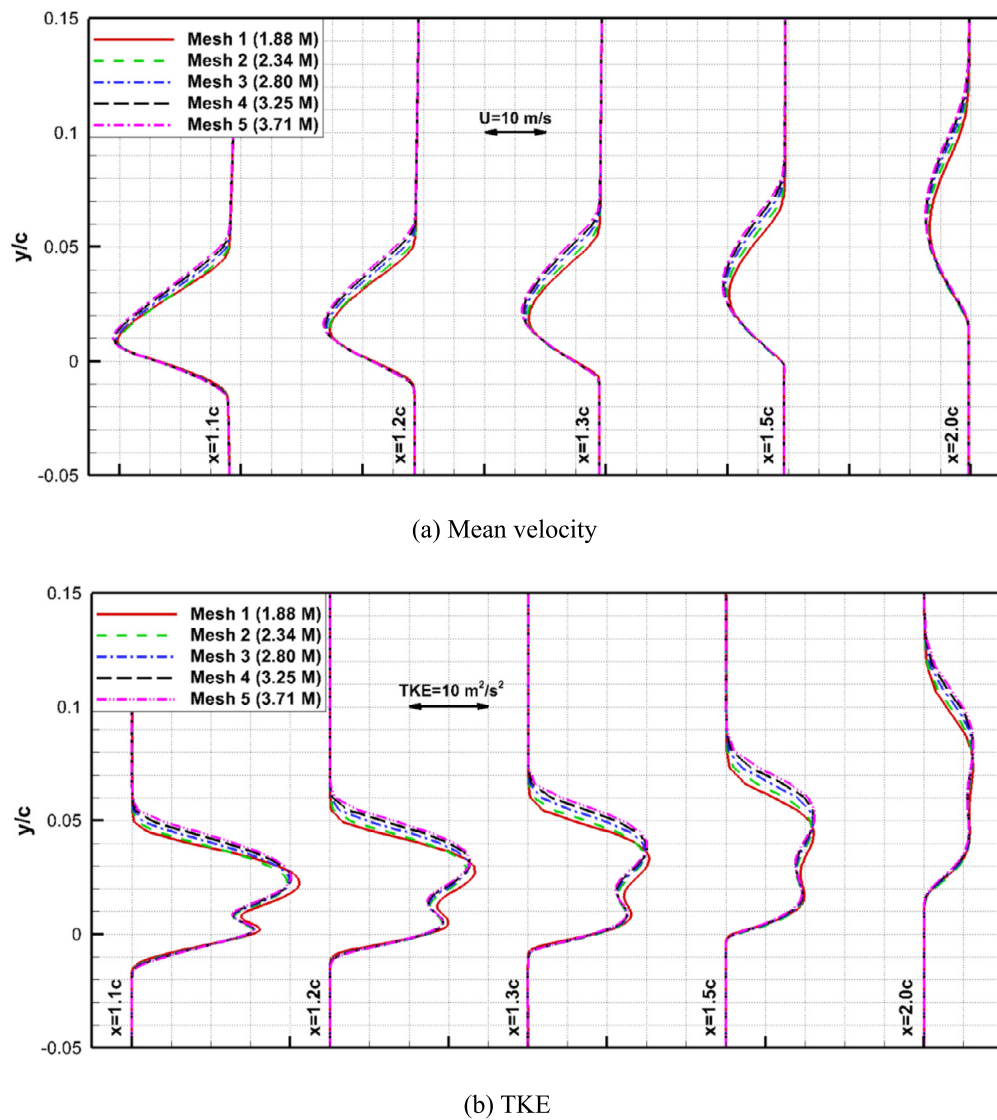


**Fig. 4.** Mesh independence study on the wake development of the A10W10 airfoil.

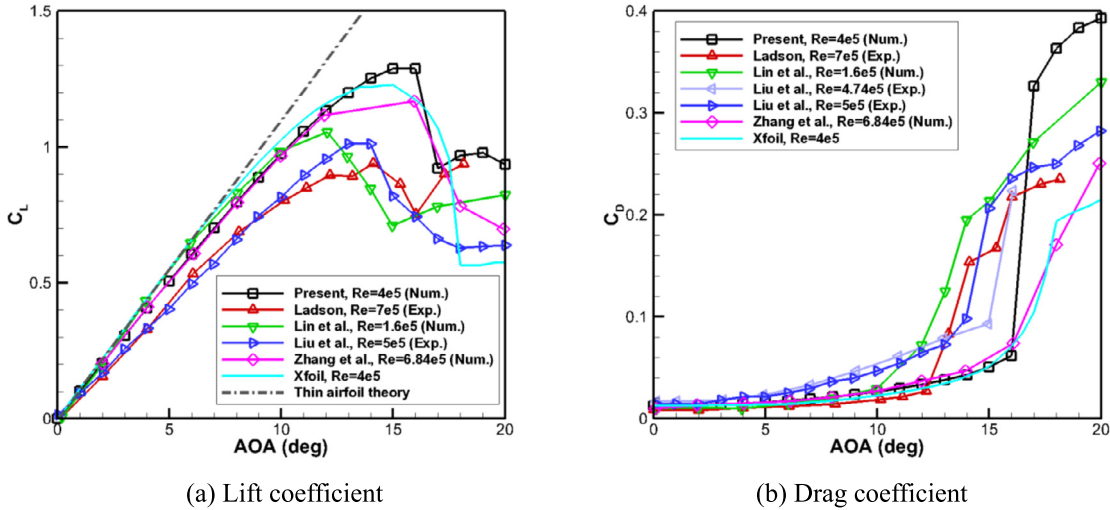


**Fig. 5.** Validation and verification of the lift and drag coefficients of the baseline airfoil.

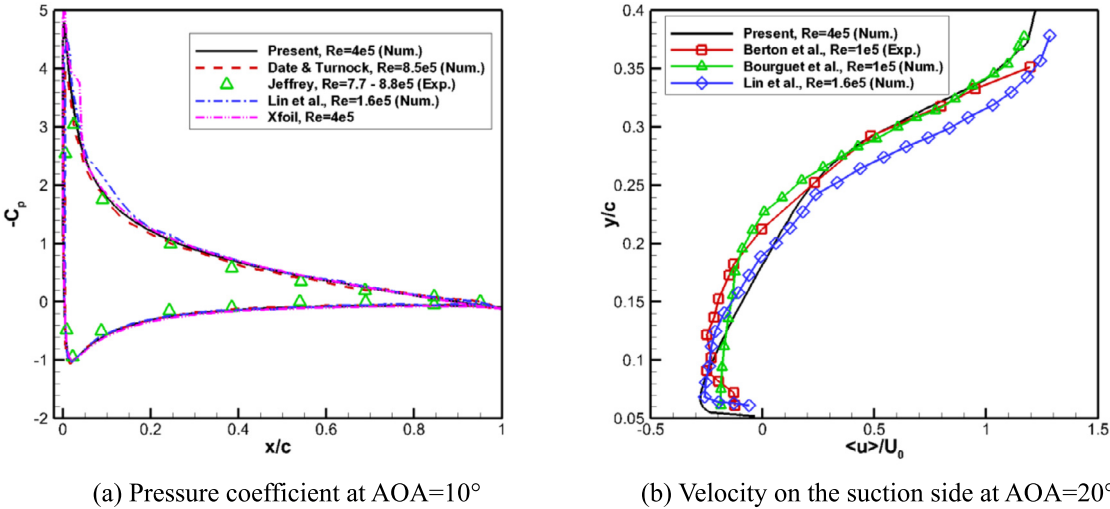


**Fig. 6.** Validation and verification of the pressure coefficient and streamwise velocity distribution of the baseline airfoil.

gent with increasing grid nodes. In particular, the computed values have insignificant discrepancies between the Mesh 4 and Mesh 5. Finally, the Mesh 4 is chosen for further analysis compromising the numerical accuracy and efficiency.

The numerical method is further validated and verified based on the baseline airfoil using Mesh 4 at various angles of attack. The computed lift coefficients are plotted in Fig. 5(a) and compared with the previous experimental and numerical data. It can be seen that the present numerical results are in close agreement with the numerical results of Lin et al. [27], Zhang et al. [53] and the panel method code XFOIL [55] for angles of attack less than  $12^\circ$ . The computed lift curve slope is approximately 0.1, which is very close to the value of 0.11 of the thin airfoil theory [56]. However, the computed lift curve slope is a little larger than the experimental data of Ladson [51] and Liu et al. [52]. In the range from  $13^\circ$  to  $17^\circ$ , the present lift coefficients match well with the numerical results of Zhang et al. and the XFOIL code. In the post-stall region, the present results agree well with the experimental data of Ladson.

The computed drag coefficients are plotted in Fig. 5(b) and compared with other results in the literature. For angles of attack less than  $10^\circ$ , the present drag coefficients are in excellent agreement with the experimental data of Ladson [51], the numerical results of Lin et al. [27], Zhang et al. [53] and the XFOIL code

[55], while the experimental data of Liu et al. [52,54] give larger drag coefficients. For angles of attack between  $12^\circ$  and  $17^\circ$ , the present results match well with the numerical results of Zhang et al. and the XFOIL code. The deviations between different methods generally increase with increasing angles of attack. In the post-stall regime, the present simulations obtain larger values compared to other methods.

However, it should be recognized that there are some differences between the various numerical and experimental data especially when the airfoil is in stall. These relatively large differences in the stall region are probably due to the different inflow turbulence level, wall roughness condition, aspect ratio of the airfoil and boundary layer tripping in the experiment. While in the numerical simulation, the used turbulence models and aspect ratio might contribute to the differences. However, the force coefficients of both the present study and previous work exhibit clear trend with the angle of attack.

The surface pressure coefficient of the baseline NACA0012 airfoil at an angle of attack of  $10^\circ$  is plotted in Fig. 6(a) and compared with previously published data. The present values agree well with the numerical results of Date et al. [57] and the experimental results of Jeffrey [58], while there are little differences with the numerical results of Lin et al. [27] and the XFOIL code on the suction side. The time-averaged streamwise velocity at half-chord

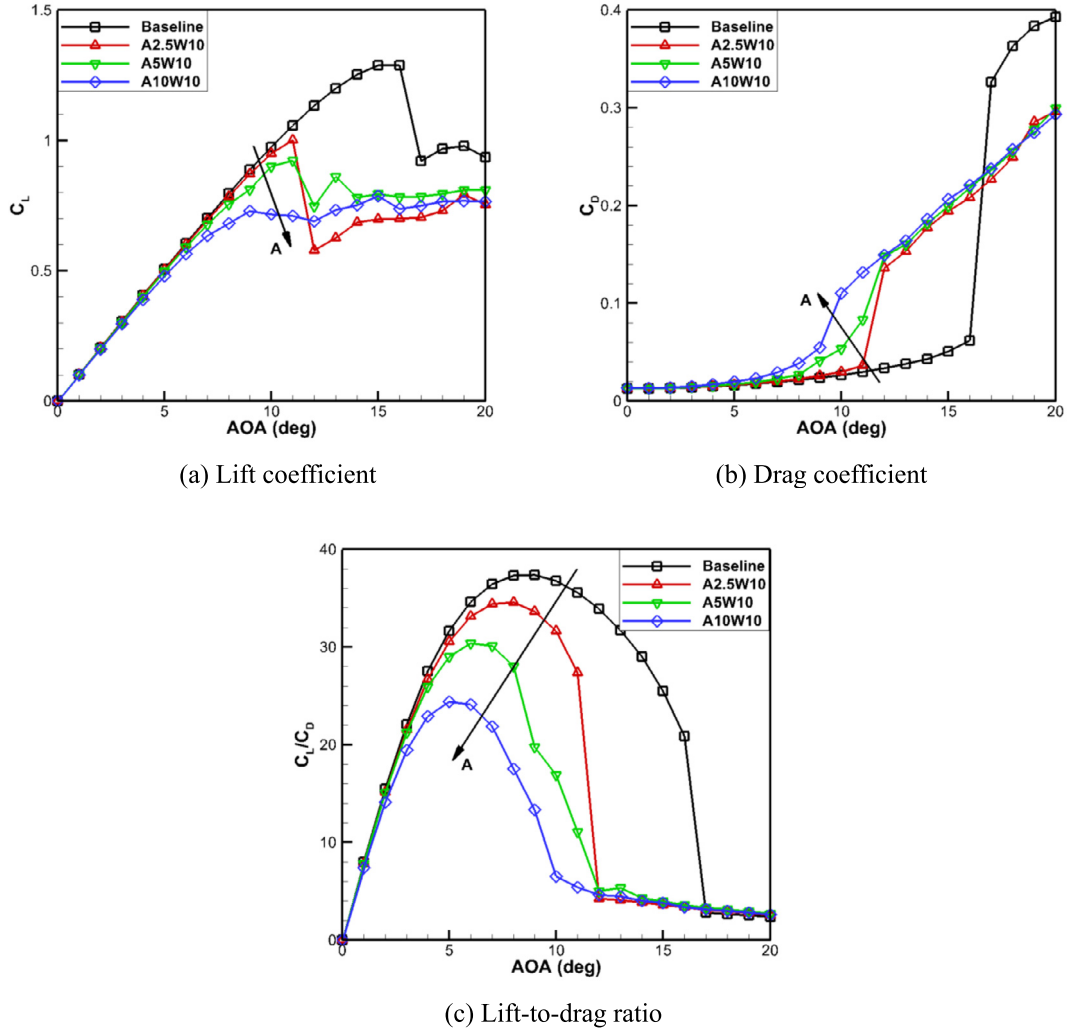


**Fig. 7.** Effect of the amplitude on the airfoil performance.

distance ( $x/c = 0.508$ ) on the suction side of the airfoil at an angle of attack of  $20^\circ$  is shown in Fig. 6(b) and compared with other experimental and numerical results. The present computed streamwise velocity distribution agrees well with the experimental results of Berton et al. [59] and the numerical data of Bourguet et al. [60] and Lin et al. [27].

#### 4. Results and discussions

##### 4.1. Force performance

###### 4.1.1. Effect of amplitude

The effects of the amplitude on the airfoil aerodynamic performance are studied in Fig. 7. Three amplitudes of  $0.025c$ ,  $0.05c$  and  $0.1c$  are used with a constant wavelength of  $0.1c$ . The lift coefficient, the drag coefficient and the lift-to-drag ratio of the wavy airfoils are compared with those of the baseline airfoil. For angles of attack less than  $5^\circ$ , the WLEs show negligible effects on the lift and drag coefficients, as plotted in Fig. 7(a) and (b). The aerodynamic performance is degraded by the WLEs with increasing angles of attack. The lift is decreased and the drag is increased for angles of attack between  $6^\circ$  and  $16^\circ$ . The wavy airfoil with larger amplitude generally produces smaller lift and larger drag. When the angles of attack are greater than the baseline airfoil stall angle of  $17^\circ$ , the lift coefficient is still decreased by the WLEs,

while the drag coefficient is also significantly decreased. For angles of attack from  $12^\circ$  to  $20^\circ$ , all the three wavy airfoils possess similar drag coefficients. It is notable that the baseline, A2.5W10 and A5W10 airfoils stall at  $17^\circ$ ,  $12^\circ$  and  $12^\circ$ , respectively, while the A10W10 airfoil has a much softer stall process without the abrupt drop of the lift coefficient. It is observed from Fig. 7(c) that a larger value of lift-to-drag ratio is obtained by the baseline airfoil compared with the wavy airfoils for angles of attack from  $5^\circ$  to  $16^\circ$ . The maximum lift-to-drag ratio and the corresponding angle of attack are decreased by the wavy airfoil. The wavy airfoil with the largest amplitude has the smallest maximum lift-to-drag ratio and corresponding attack angle. For angles of attack greater than the baseline stall angle of  $17^\circ$ , the baseline airfoil generates the same lift-to-drag ratio with the wavy airfoils. It is also worth noting that the lift-to-drag ratios have insignificant difference for the three wavy airfoils for angles of attack from  $12^\circ$  to  $17^\circ$ .

###### 4.1.2. Effect of wavelength

The effects of the wavelength on the airfoil aerodynamic performance are shown in Fig. 8. Three wavelengths of  $0.1c$ ,  $0.2c$  and  $0.4c$  are studied with constant amplitude of  $0.1c$ . It can be seen from Fig. 8(a) and (b) that the lift and drag coefficients of the wavy airfoil are in general consistent with the baseline airfoil for angles of attack smaller than  $5^\circ$ . The lift is decreased and the drag is increased from  $6^\circ$  to  $16^\circ$ . In contrast to the effect of the ampli-

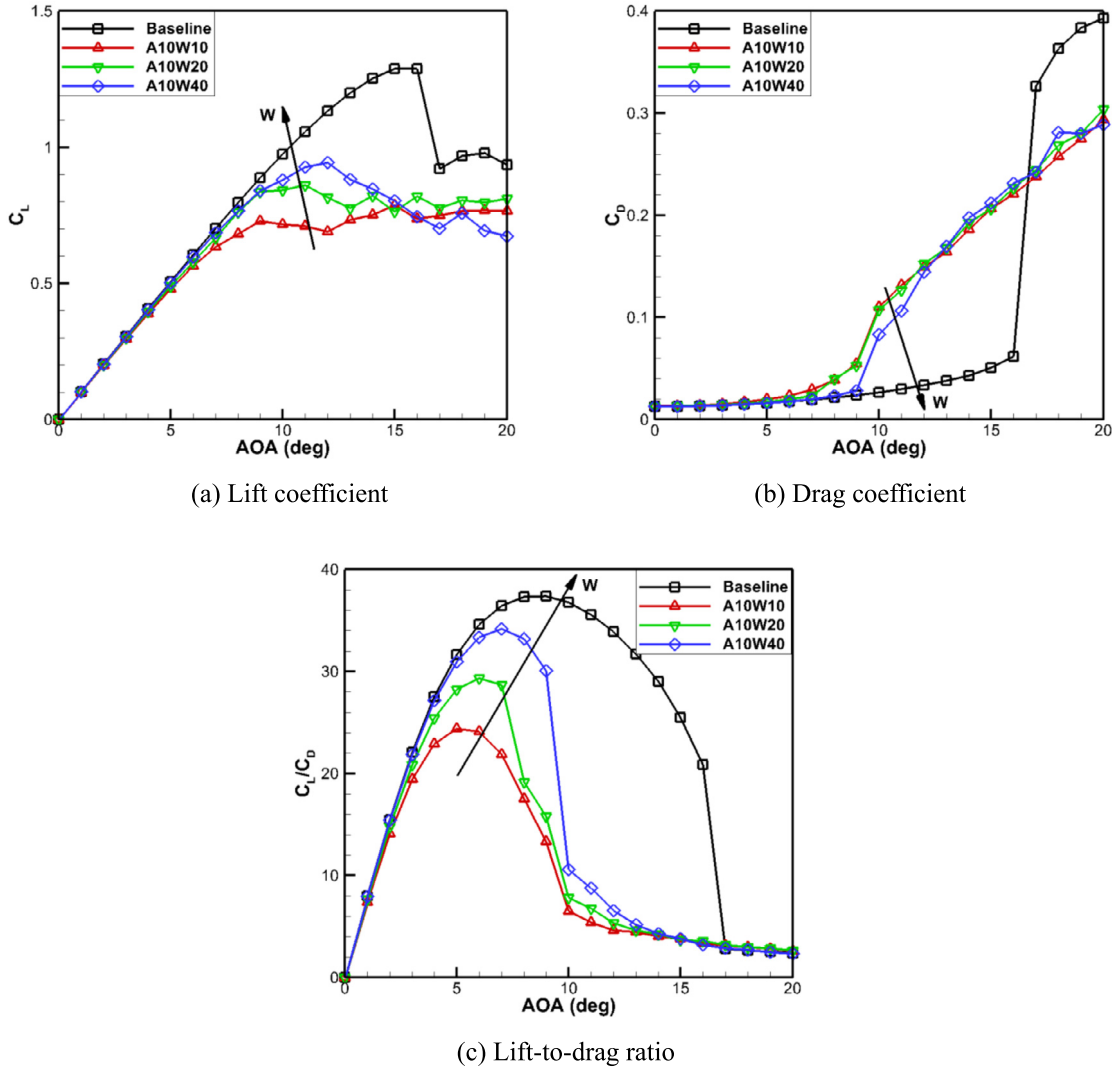


**Fig. 8.** Effect of the wavelength on the airfoil performance.

tude, the wavy airfoil with a larger wavelength generally generates larger lift and smaller drag. After the baseline stall angle of  $17^\circ$ , the lift is still decreased by the WLEs, while the drag is also significantly mitigated. For angles of attack from  $12^\circ$  to  $20^\circ$ , all the three wavy airfoils have similar drag coefficients. It is also notable that all the three wavy airfoils have a much softer stall process without the abrupt drop of the lift coefficient. It can be observed from Fig. 8(c) that the WLEs show negligible influences on the lift-to-drag ratio for angles of attack less than  $5^\circ$ . However, it is reduced in the range from  $5^\circ$  to  $16^\circ$ . The wavy airfoils produce the same values of lift-to-drag ratio after the baseline stall angle. The maximum lift-to-drag ratio and the corresponding attack angle are degraded by the wavy airfoil. The wavy airfoil with the largest wavelength has the largest maximum lift-to-drag ratio and related attack angle. It is also notable that the lift-to-drag ratios have insignificant difference for the three wavy airfoils for angles of attack from  $13^\circ$  to  $17^\circ$ .

Fig. 9 shows the time history of the lift and drag coefficients for the various airfoils at an angle of attack of  $17^\circ$ . It is observed that both the lift and drag coefficients are reduced by the wavy airfoils. In the meanwhile, the fluctuations of the lift and drag are also reduced by the wavy airfoils, which might indicate that the wavy airfoils can be used for noise control, because the far-field sound radiation is related to the force fluctuations on the airfoil

surface. Recent experimental studies by Lacagnina et al. [34,35] also confirmed that the WLEs can be used for separation-stall noise suppression.

The aerodynamic characteristics including the lift curve slope ( $dC_L/d\alpha$ ), the maximum lift coefficient ( $C_{L,\max}$ ), the angle of maximum lift coefficient, the maximum lift-to-drag ratio ( $(C_L/C_D)_{\max}$ ), the angle of maximum lift-to-drag ratio and the stall angle for all the airfoils studied are summarized in Table 4. The lift curve slope is computed within the linear range. It can be seen that all the wavy airfoils have a lower lift curve slope than the baseline airfoil. Moreover, the lift curve slope of the wavy airfoil generally decreases with increasing amplitude, while increases with increasing wavelength. The lowest lift curve slope of 0.087 is obtained for the A10W10 airfoil. The maximum lift coefficient and lift-to-drag ratio are also reduced by the wavy airfoil. Moreover, the maximum lift coefficient and lift-to-drag ratio of the wavy airfoil also decreases with increasing amplitude, while increases with increasing wavelength. The lowest maximum lift coefficient of 0.79 and the lowest maximum lift-to-drag ratio of 24.4 are found for the A10W10 airfoil, leading to a decrease of 38.8% and 34.8% compared to those of the baseline airfoil. The corresponding angles of attack are also reduced by the wavy airfoil. The stall angles for the A10W10, A10W20 and A10W40 airfoils are not listed because they do not stall in the traditional manner.

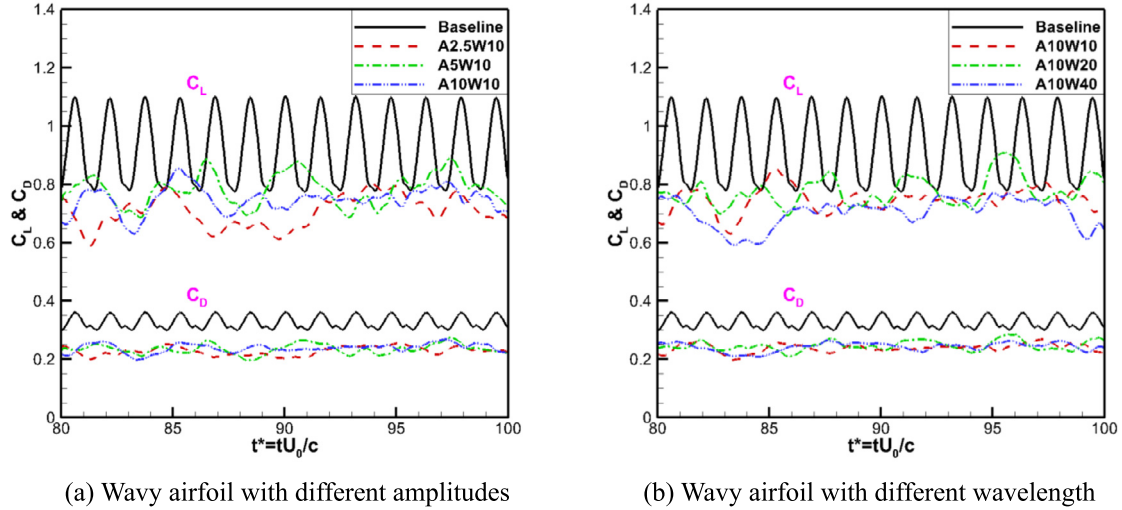


**Fig. 9.** Time history of the lift and drag coefficients of the various airfoils at  $\text{AOA} = 17^\circ$ .

**Table 4**  
Aerodynamic characteristics of the baseline and wavy airfoils.

Airfoil	$dC_L/d\alpha$	$C_{L,\max}$	$\text{AOA at } C_{L,\max} (\text{°})$	$(C_L/C_D)_{\max}$	$\text{AOA at } (C_L/C_D)_{\max} (\text{°})$	Stall AOA (°)
Baseline	0.094	1.29	16	37.4	9	17
A2.5W10	0.093	1.00	11	34.6	8	12
A5W10	0.090	0.92	11	30.4	6	12
A10W10	0.087	0.79	15	24.4	5	—
A10W20	0.093	0.86	11	29.4	6	—
A10W40	0.091	0.94	12	34.2	7	—

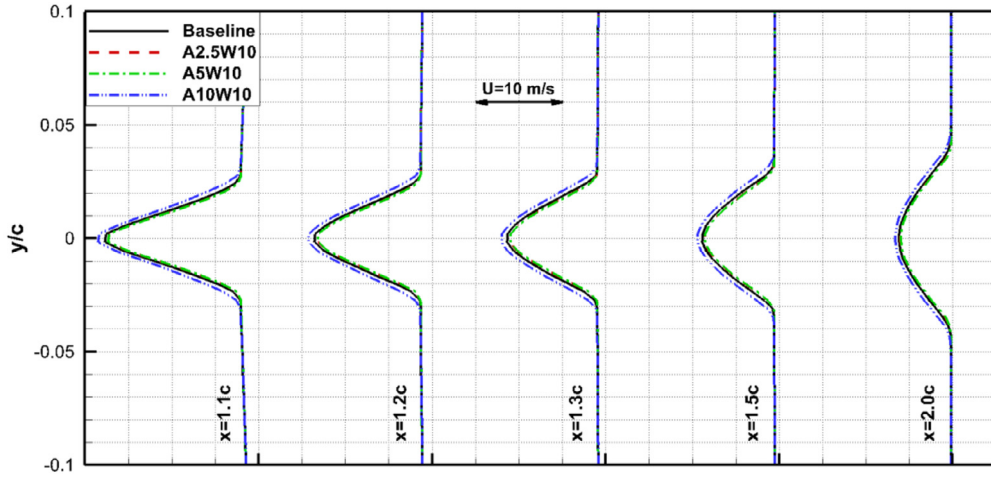


**Fig. 10.** Effect of amplitude: wake development at  $\text{AOA} = 0^\circ$ .

#### 4.2. Wake characteristics

In this section, detailed wake flow analyses are performed at several downstream locations to better understand the effects of wavy airfoil on the wake development. The effects of amplitude and wavelength on wake development are studied for angles of attack of  $0^\circ$ ,  $5^\circ$ ,  $10^\circ$ ,  $15^\circ$  and  $20^\circ$ .

##### 4.2.1. Effect of amplitude

The wake streamwise velocity and TKE profiles at an angle of attack of  $0^\circ$  are presented in Fig. 10 for the baseline airfoil and wavy airfoils with different amplitudes. The profiles are shown at both the corresponding peak and trough positions. It can be ob-

served from Figs. 10(a) and (b) that the wake profiles of the wavy airfoils are similar to that of the baseline in terms of both wake width and intensity. The A10W10 airfoil has a slightly higher velocity deficit at the peak, while the A2.5W10 and A5W10 airfoils have slightly higher velocity deficit at the trough in the near-wake region. Regarding the TKE shown in Figs. 10(c) and (d), a double-peak behavior is observed for both the baseline and wavy airfoils, which is due to the different velocity gradients in the boundary layers of the airfoil's upper and lower surfaces. The minimum point in the TKE between the two peaks corresponds to the position of the largest velocity deficit. The wavy airfoils have negligible influence on the TKE distribution in terms of both the magnitude and peak positions. The TKE is slightly increased by the A10W10 airfoil

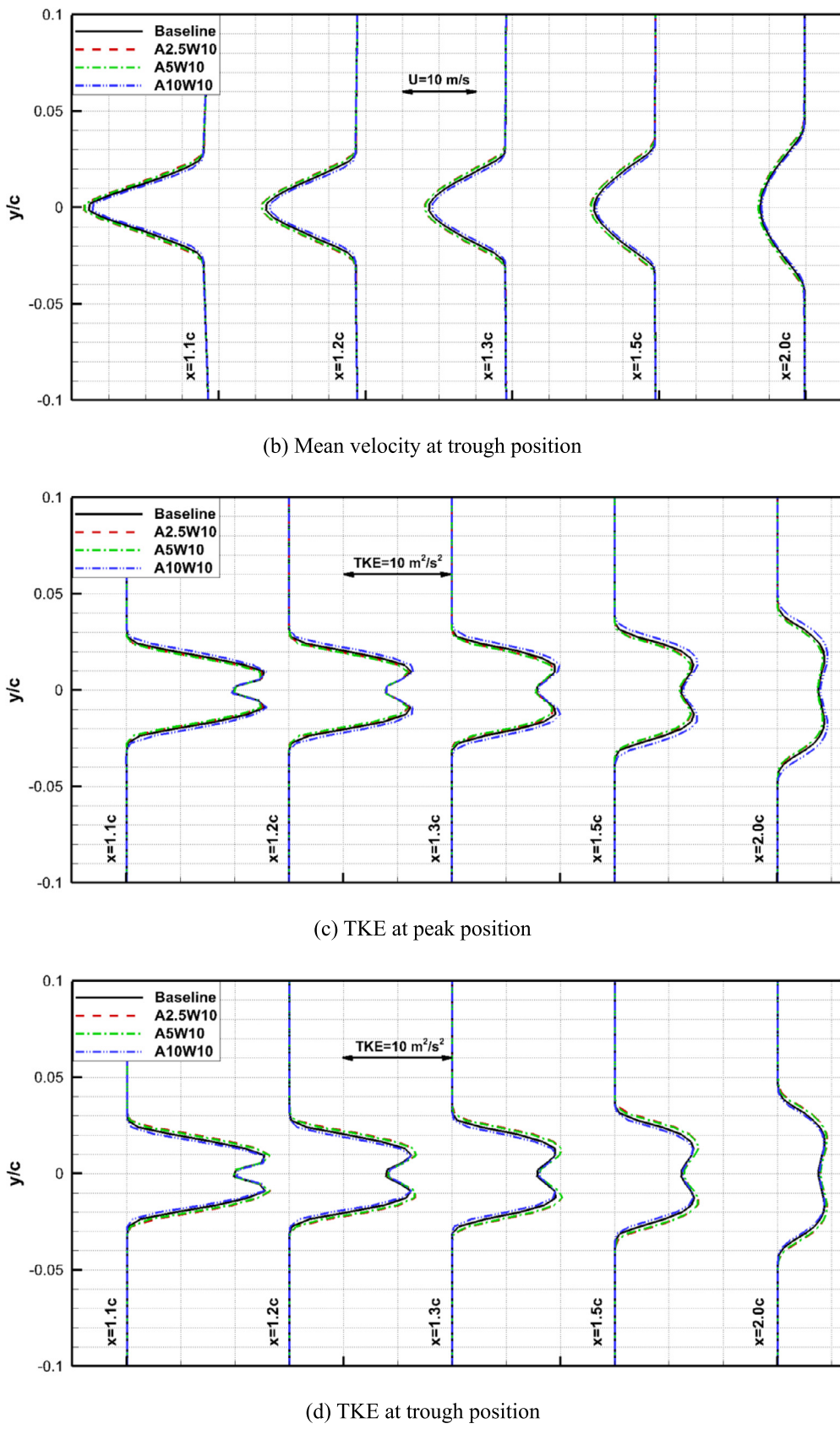


Fig. 10. (continued)

at peak position and by the A2.5W10 and A5W10 airfoils at trough position.

The wake velocity and TKE profiles at an angle of attack of 5° are plotted in Fig. 11 for the baseline airfoil and wavy airfoils with different amplitudes. Regarding the mean velocity, the A2.5W10 and A5W10 airfoils have a lower wake deficit, while the A10W10 airfoil has a higher deficit at the peak position. However, at the trough position, all the three wavy airfoils achieve a higher velocity deficit and the wavy airfoil with larger amplitude generally get larger wake deficit. Regarding the TKE shown in Figs. 11(c) and (d), a double-peak behavior is observed for both the baseline and wavy airfoils. At the peak position, the TKE is slightly decreased by the A2.5W10 and A5W10 airfoils and increased by the A10W10 airfoil. At the trough position, the TKE is increased by all the three wavy airfoils and the wavy airfoil with larger amplitude generally obtains higher TKE. In addition, the TKE peak positions are slightly shifted towards the suction side by the wavy airfoils. In general, the wavy airfoils have insignificant effects on the wake development at small angles of attack, which is in consistent with the force shown in Fig. 7.

The wake velocity and TKE profiles at an angle of attack of 10° are presented in Fig. 12 for the baseline airfoil and wavy airfoils with different amplitudes. It can be observed from Figs. 12(a) and (b) that the A2.5W10 airfoil has similar velocity profiles to that of the baseline case, while the A5W10 and A10W10 airfoils exhibit a very different behavior. The A5W10 airfoil has the same maximum velocity deficit with the baseline airfoil while it possesses a larger wake width. The A10W10 airfoil has a much larger wake deficit and width compared to those of the baseline case, especially in the near-wake region. Regarding the TKE distribution shown in Figs. 12(c) and (d), a double-peak behavior is observed for both the baseline and A2.5W10 airfoils except for the farthest downstream position. However, very weak double-peak behavior is observed for the A5W10 airfoil and only one-peak is found for the A10W10 airfoil. The A2.5W10 airfoil has similar TKE distribution to the baseline airfoil. The TKE is slightly increased by the A5W10 airfoil, while it is significantly increased by the A10W10 airfoil. The large wake deficit of the A10W10 airfoil at this flow condition indicates a decrease of the aerodynamic performance, as shown in Fig. 7.

The wake velocity and TKE profiles at an angle of attack of 15° are shown in Fig. 13 for the baseline airfoil and wavy airfoils with different amplitudes. Contrary to the lower angles of attack, all the wavy airfoils possess higher wake deficit compared to that of the baseline airfoil. Both the maximum velocity deficit and wake width are significantly increased by the wavy airfoils. In addition, the velocity profiles have no obvious difference for the three wavy airfoils, as shown in Figs. 13(a) and (b). The TKE is significantly increased by the A2.5W10 airfoil, while the A5W10 and A10W10 airfoils have comparable values of maximum TKE compared to that of the baseline airfoil. However, the overall TKE of these two airfoils is higher than the baseline airfoil.

The wake velocity and TKE profiles at an angle of attack of 20° are shown in Fig. 14 for the baseline airfoil and wavy airfoils with different amplitudes. Very different features are observed in this post-stall regime. The wake is shifted towards the pressure side by the wavy airfoils, especially in the near-wake region. All the three wavy airfoils have a higher velocity deficit and wake width compared to the baseline airfoil. However, the TKE is significantly reduced by the wavy airfoils. The baseline airfoil has a double-peak distribution of the TKE, while the wavy airfoils only have one peak near the pressure side. In general, there are no obvious differences for the three wavy airfoils in terms of both velocity and TKE distributions. It can be found from Figs. 12–14 that the wavy airfoil only affects the wake development on the suction side, while

it has negligible effect on the wake development on the pressure side.

#### 4.2.2. Effect of wavelength

The wake streamwise velocity and TKE profiles at an angle of attack of 0° are presented in Fig. 15 for the baseline airfoil and wavy airfoils with different wavelengths. The wake profiles for the wavy airfoils are generally similar to those of the baseline airfoil. It can be observed from Figs. 15(a) and (c) that the wake deficit and TKE intensity are slightly increased by the A10W10 airfoil at the peak position, while the A10W20 and A10W40 airfoils have slightly higher wake deficit and TKE at the trough position, as shown in Figs. 15(b) and (d).

The wake velocity and TKE profiles at an angle of attack of 5° are presented in Fig. 16 for the baseline airfoil and wavy airfoils with different wavelengths. At the peak position, the A10W10 airfoil has a slightly higher wake deficit and TKE intensity, while the A10W20 and A10W40 airfoils have slightly lower wake deficit and TKE, as shown in Figs. 16(a) and (c). At the trough position, very distinct phenomena are observed. The wake deficit and TKE are increased by all the three wavy airfoils. This is believed to be caused by the higher adverse pressure gradient behind the trough region. In addition, the wake is slightly shifted towards the pressure side by the wavy airfoil at the peak position, while it is slightly shifted towards the suction side at the trough position, especially for the wavy airfoils with large wavelengths.

The wake velocity and TKE profiles at an angle of attack of 10° are plotted in Fig. 17 for the baseline airfoil and wavy airfoils with different wavelengths. At this flow condition, similar trends are observed at the peak and trough positions. The wake deficit is increased and the wake is shifted towards the suction side by all the three wavy airfoils at both the peak and trough positions. The wavy airfoil with larger wavelength generally has a lower maximum velocity deficit in the near-wake region. However, the differences of the three airfoils tend to be insignificant in the further downstream due to wake mixing. The TKE in the near-wake region is significantly increased by the wavy airfoils and the wavy airfoil with smaller wavelength causes more TKE enlargement. The A10W20 and A10W40 airfoils have a lower maximum TKE compared to that of the baseline airfoil, as shown in Figs. 17(b) and (d).

The wake velocity and TKE profiles at an angle of attack of 15° are presented in Fig. 18 for the baseline airfoil and wavy airfoils with different wavelengths. It is found from Figs. 18(a) and (b) that, all the wavy airfoils have higher wake deficit compared to that of the baseline at both the peak and trough positions. Both the wake intensity and width are significantly increased by the wavy airfoils. The TKE is also significantly increased by the three airfoils at both the peak and trough positions. It is notable that the maximum TKE is increased by the wavy airfoils in the near-wake region ( $x/c = 1.1, 1.2$ ), while it is decreased in the far-wake region. In general, wake profiles have no obvious differences for the three wavy airfoils with different wavelengths.

The wake velocity and TKE profiles at an angle of attack of 20° are further shown in Fig. 19 for the baseline airfoil and wavy airfoils with different wavelengths. In this post-stall regime of the baseline airfoil, all the three wavy airfoils have a higher velocity deficit and wake width compared to the baseline at both the peak and trough positions. The wake is shifted towards the pressure side by the wavy airfoils. The TKE is significantly reduced at both the peak and trough positions for the wavy airfoils with smaller wavelength. For the A10W40 airfoil with the largest wavelength, the TKE is reduced in the very near-wake region ( $x/c = 1.1$ ). However, it exceeds the baseline airfoil at further downstream locations.

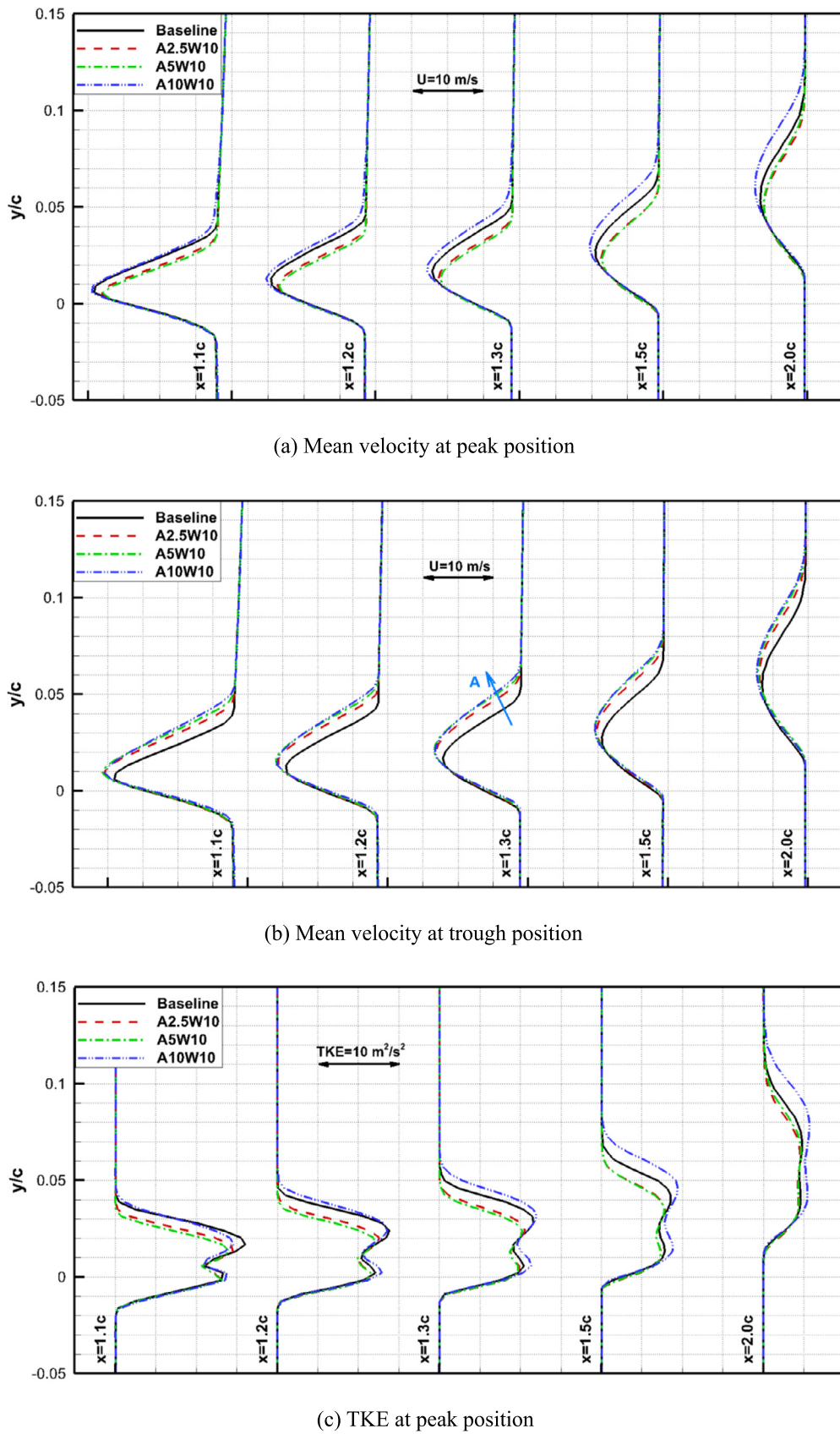
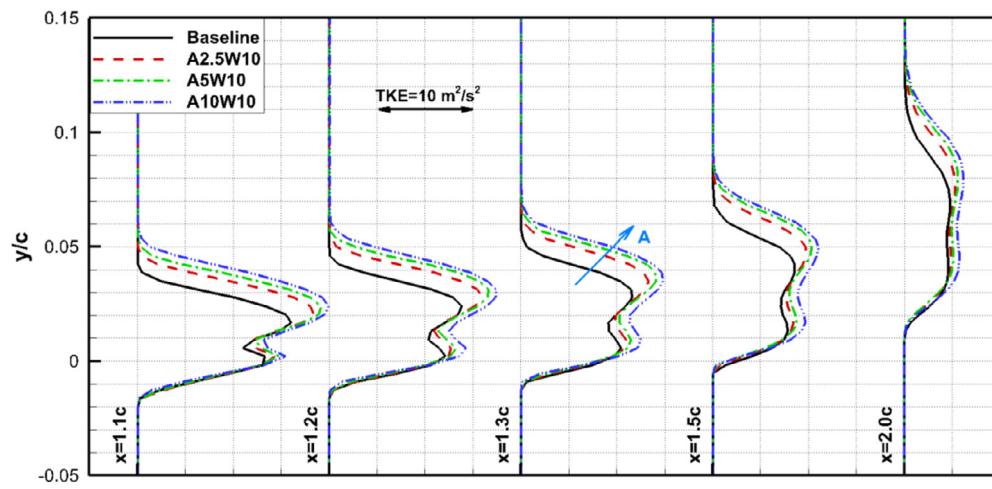
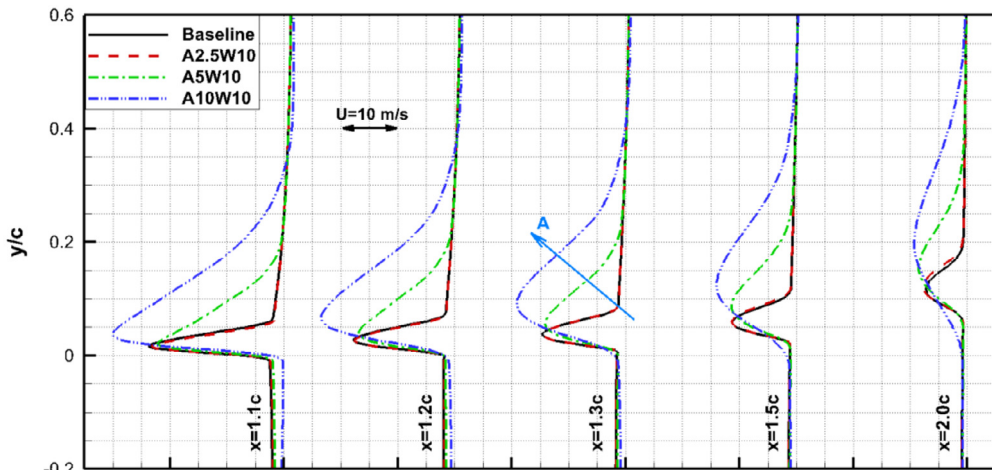


**Fig. 11.** Effect of amplitude: wake development at AOA = 5°.

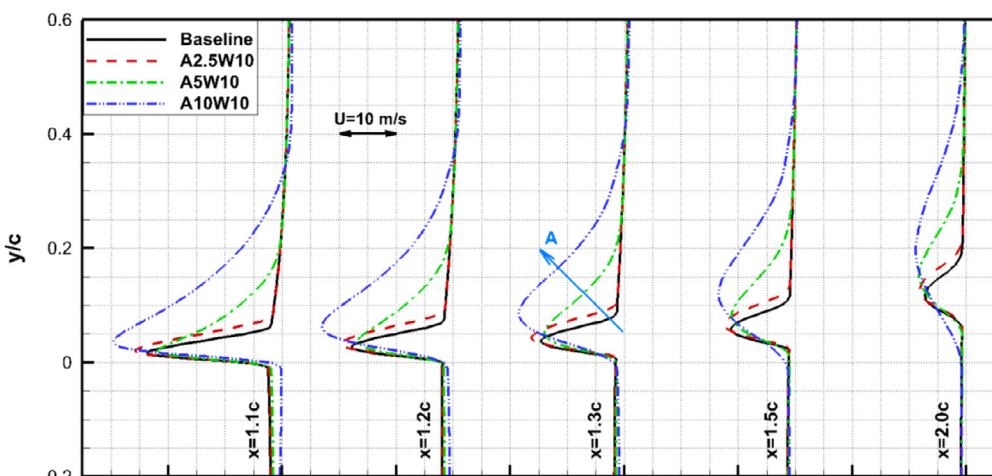


(d) TKE at trough position

Fig. 11. (continued)

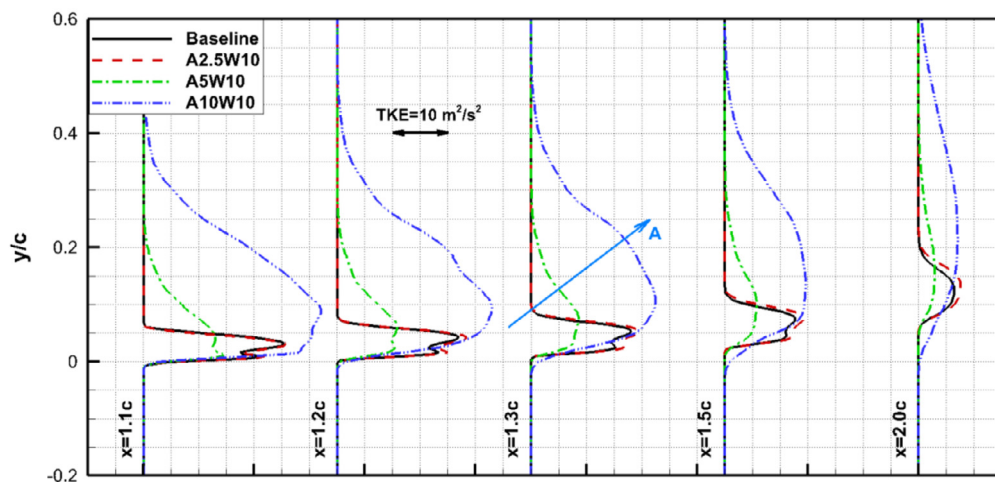


(a) Mean velocity at peak position

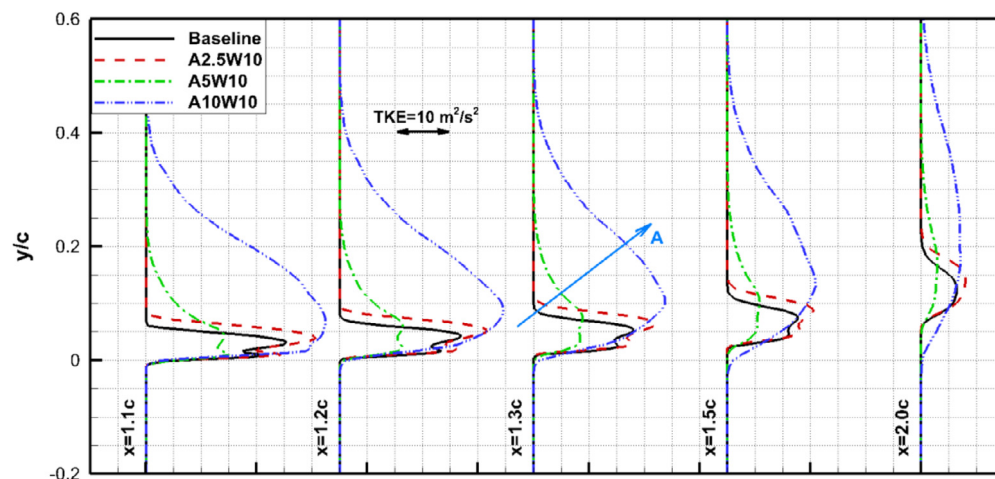


(b) Mean velocity at trough position

Fig. 12. Effect of amplitude: wake development at AOA = 10°.

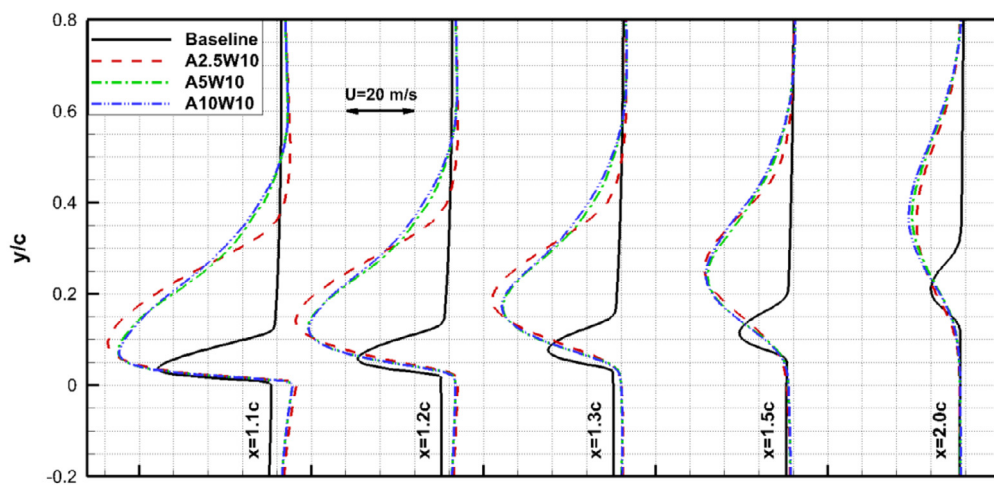


(c) TKE at peak position



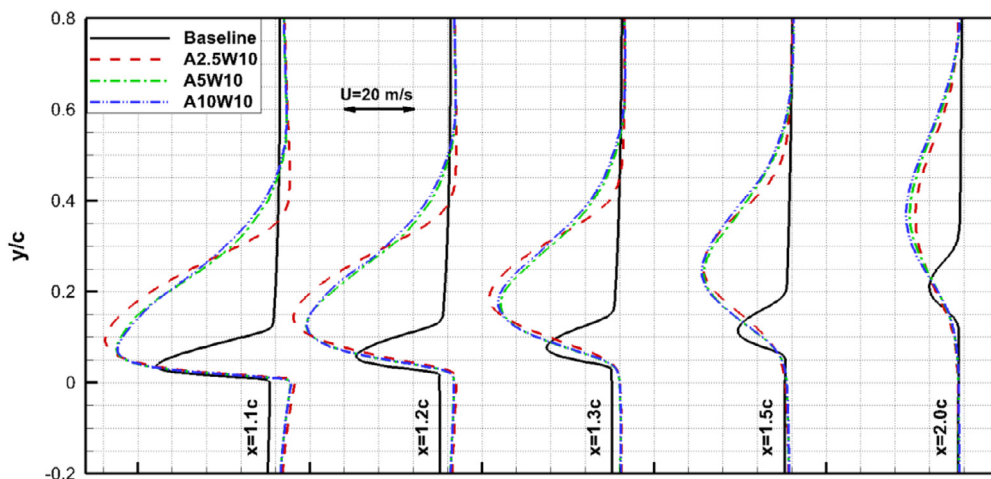
(d) TKE at trough position

Fig. 12. (continued)

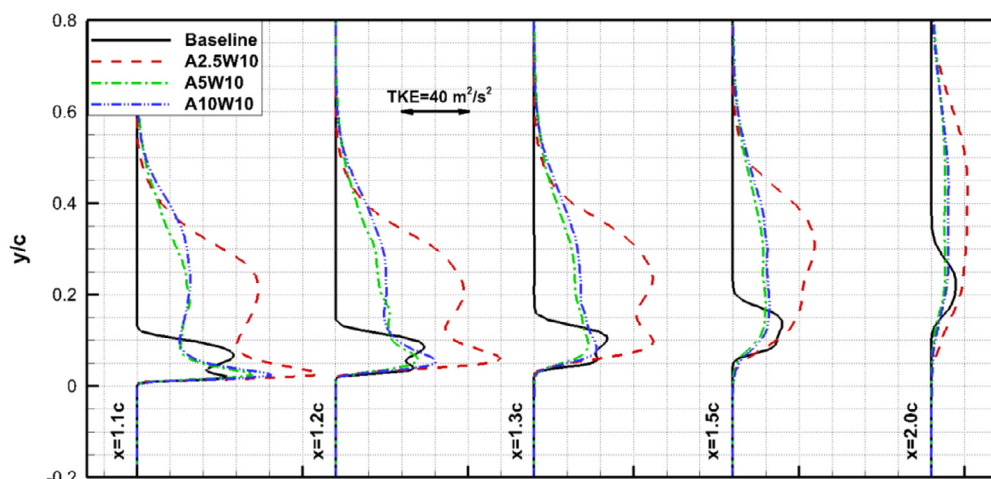


(a) Mean velocity at peak position

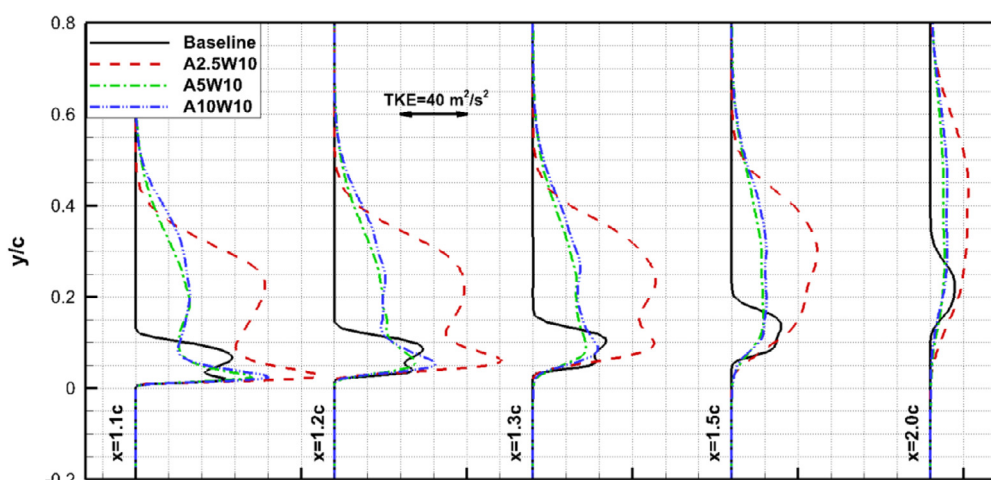
Fig. 13. Effect of amplitude: wake development at AOA = 15°.



(b) Mean velocity at trough position



(c) Turbulent kinetic energy at peak position



(d) Turbulent kinetic energy at peak position

Fig. 13. (continued)

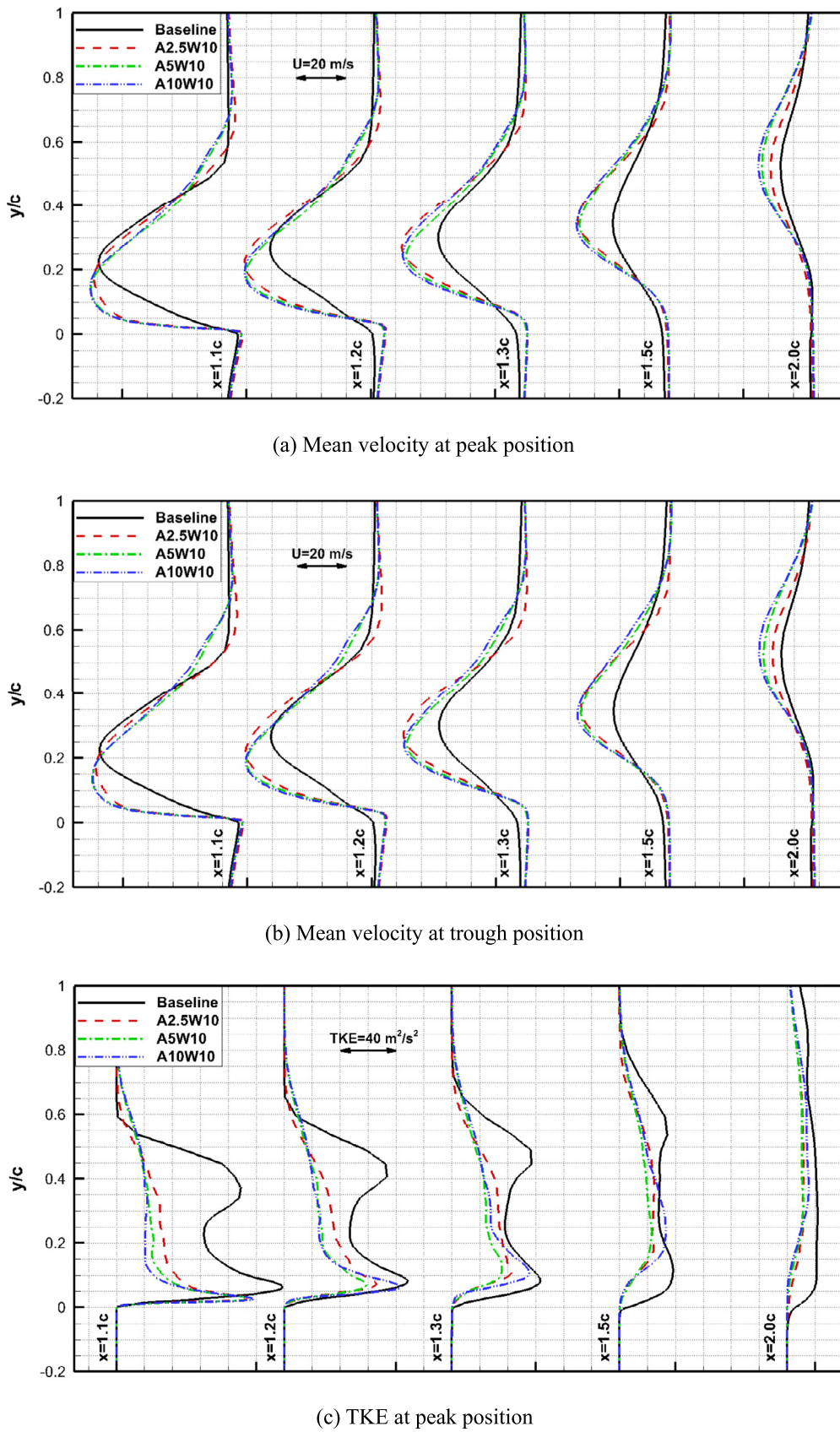
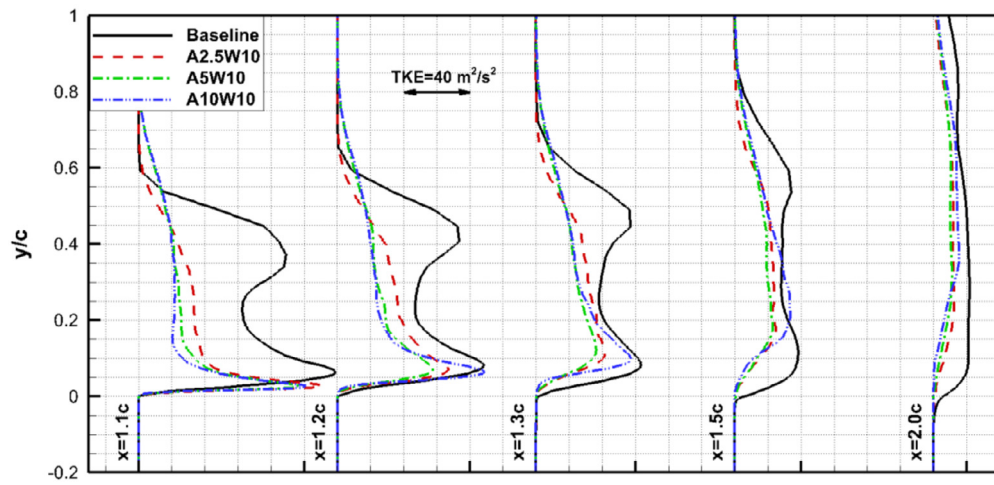
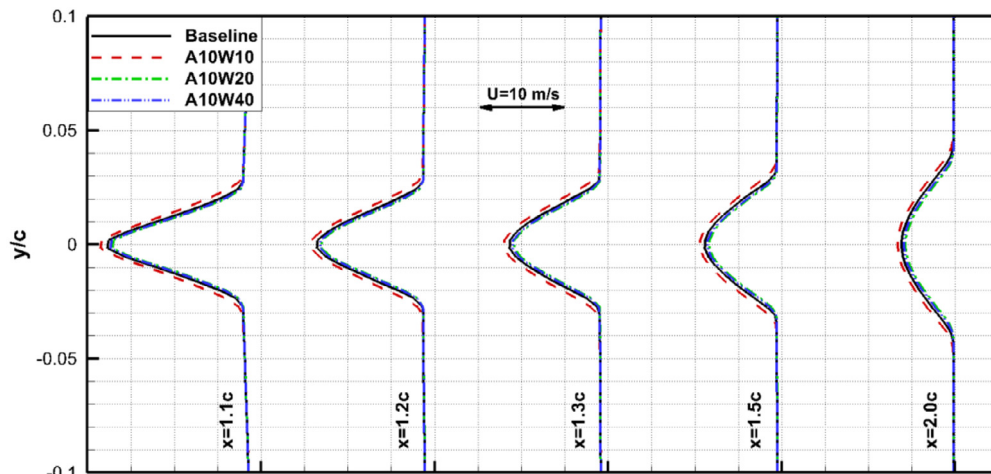


**Fig. 14.** Effect of amplitude: wake development at AOA = 20°.

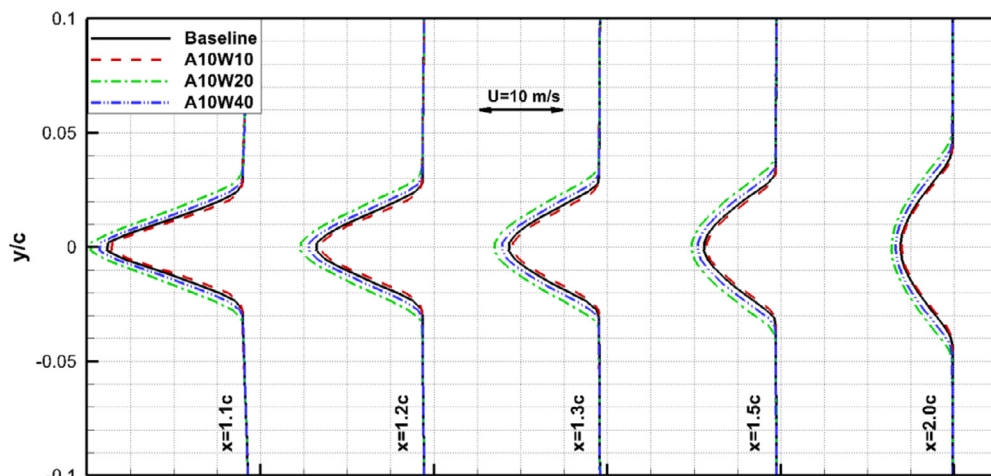


(d) TKE at peak position

Fig. 14. (continued)

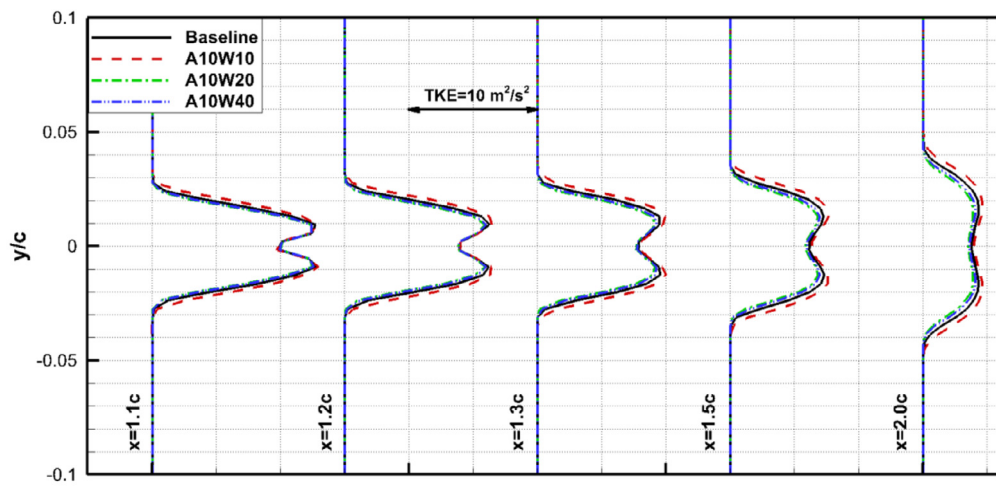


(a) Mean velocity at peak position

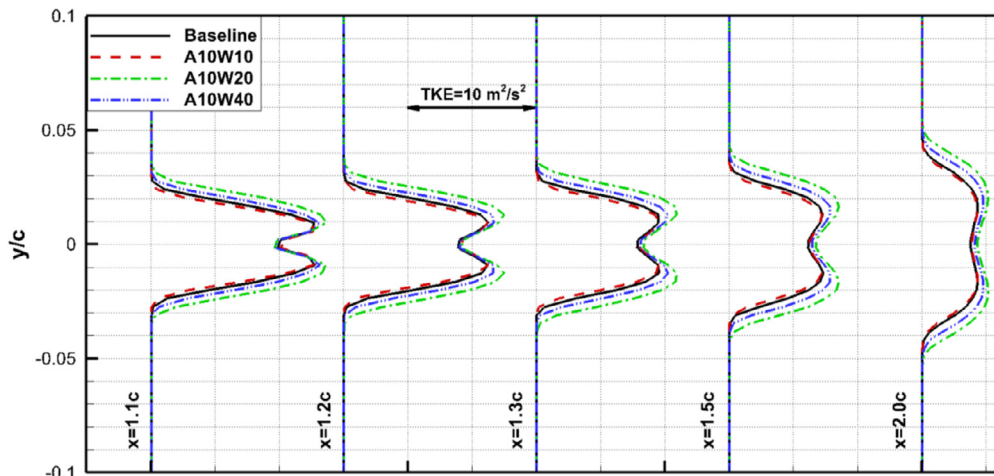


(b) Mean velocity at trough position

Fig. 15. Effect of wavelength: wake development at AOA = 0°.

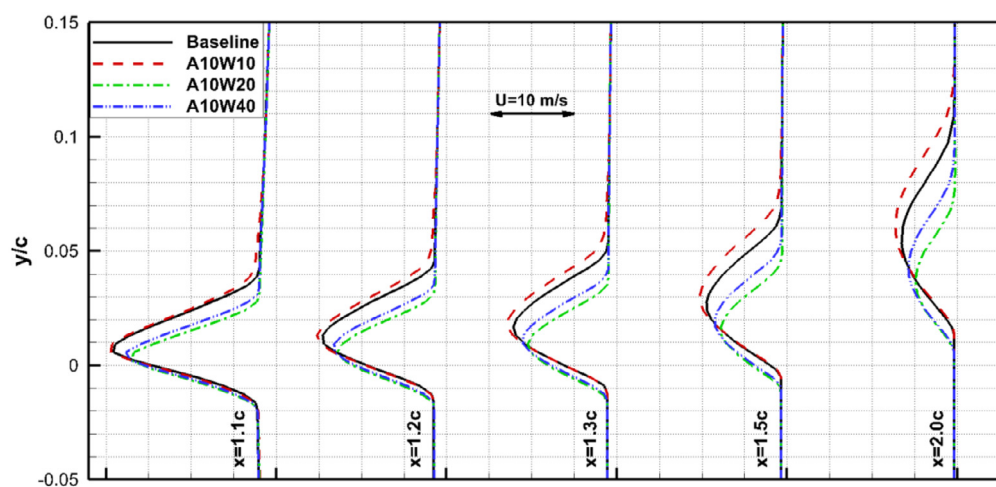


(c) TKE at peak position



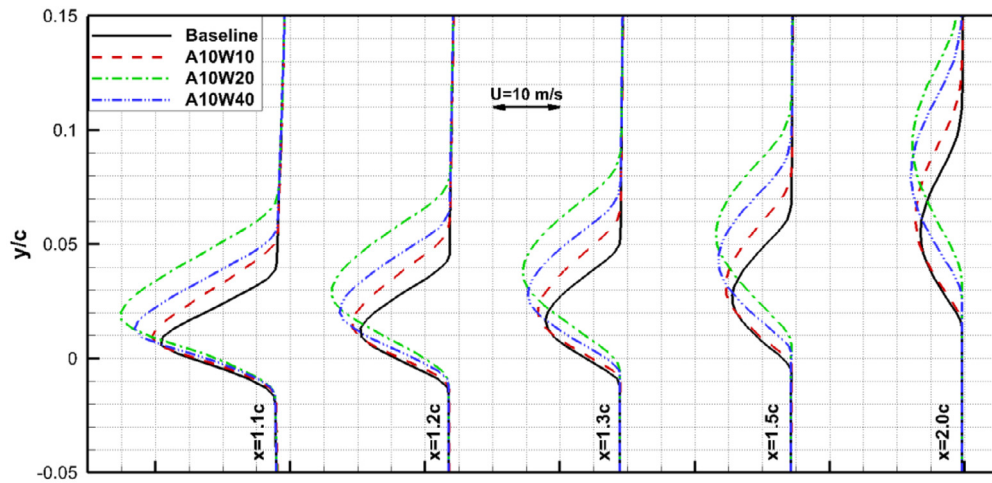
(d) TKE at trough position

Fig. 15. (continued)

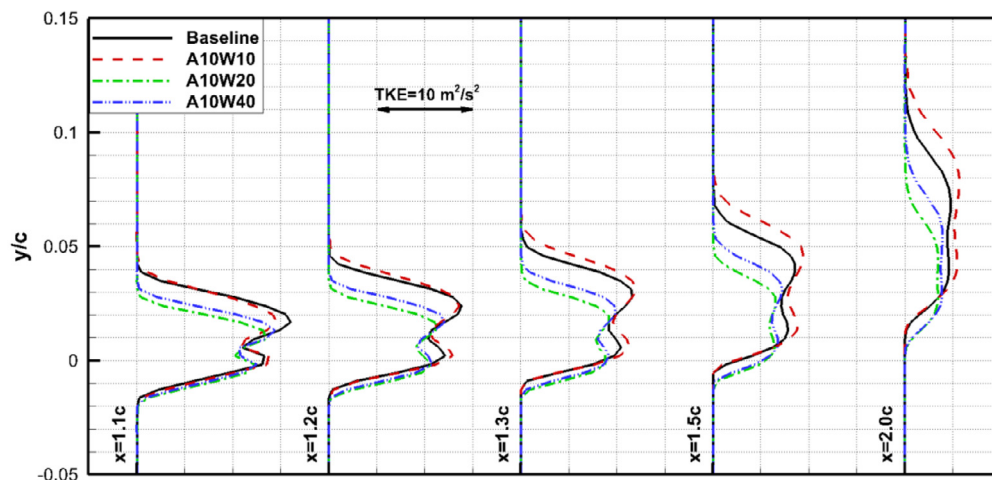


(a) Mean velocity at peak position

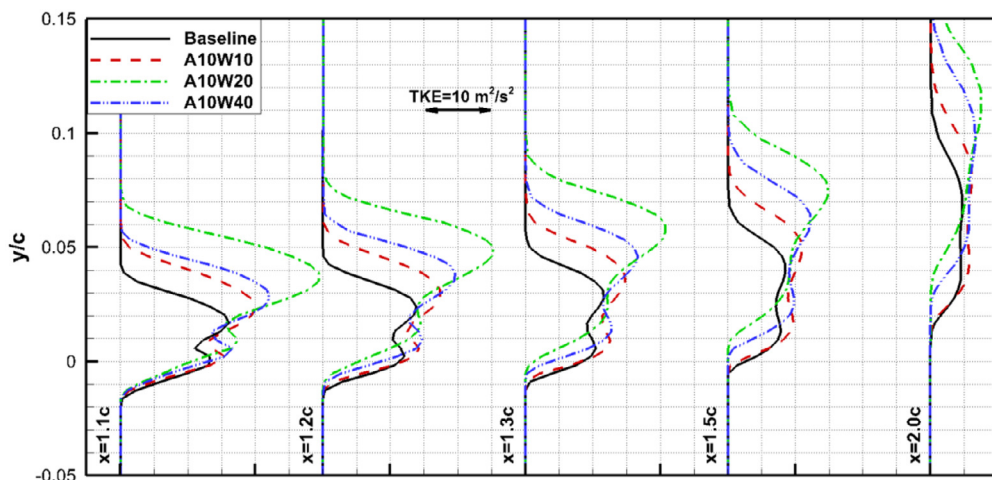
Fig. 16. Effect of wavelength: wake development at AOA = 5°.



(b) Mean velocity at trough position



(c) TKE at peak position



(d) TKE at trough position

Fig. 16. (continued)

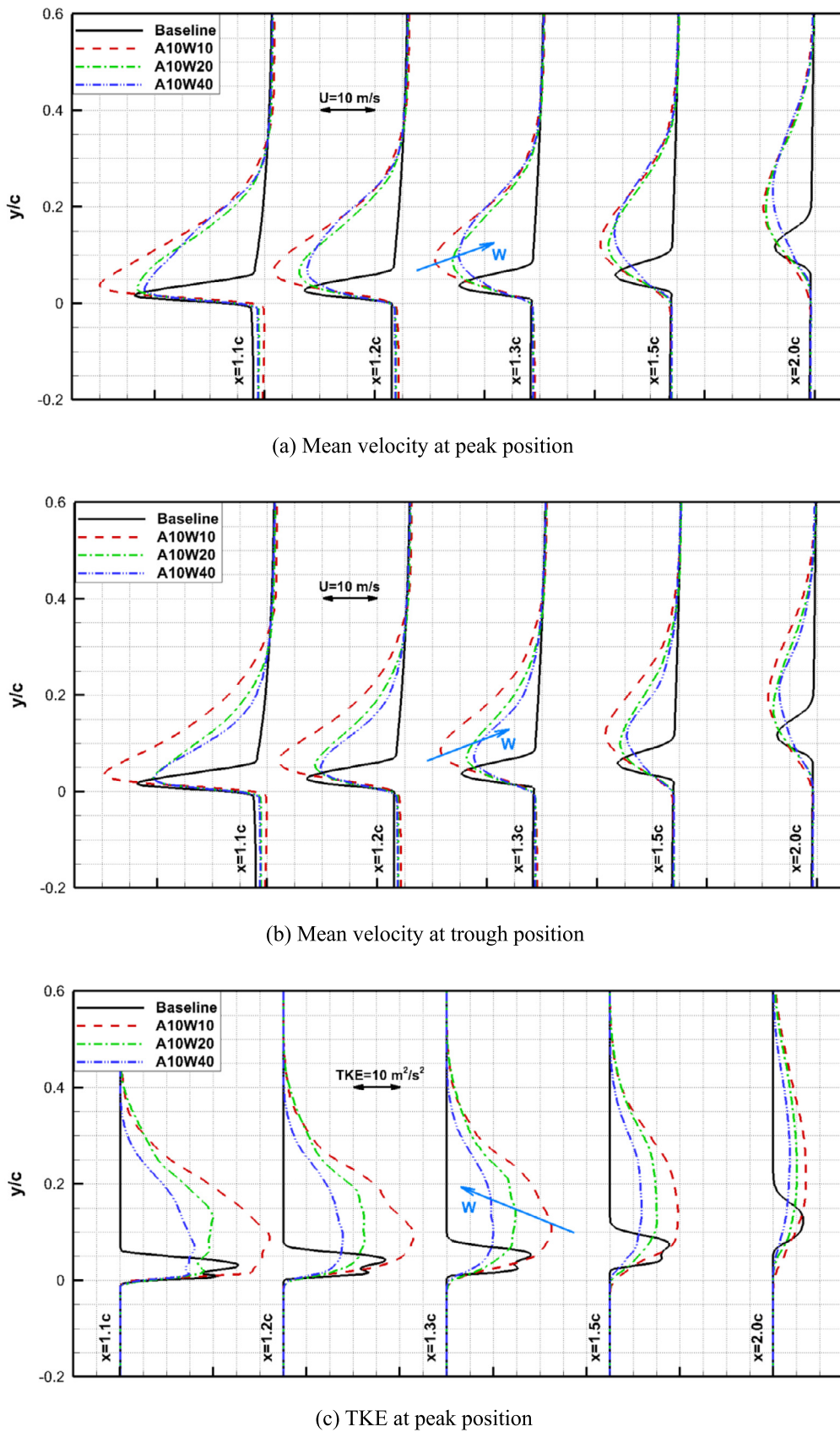
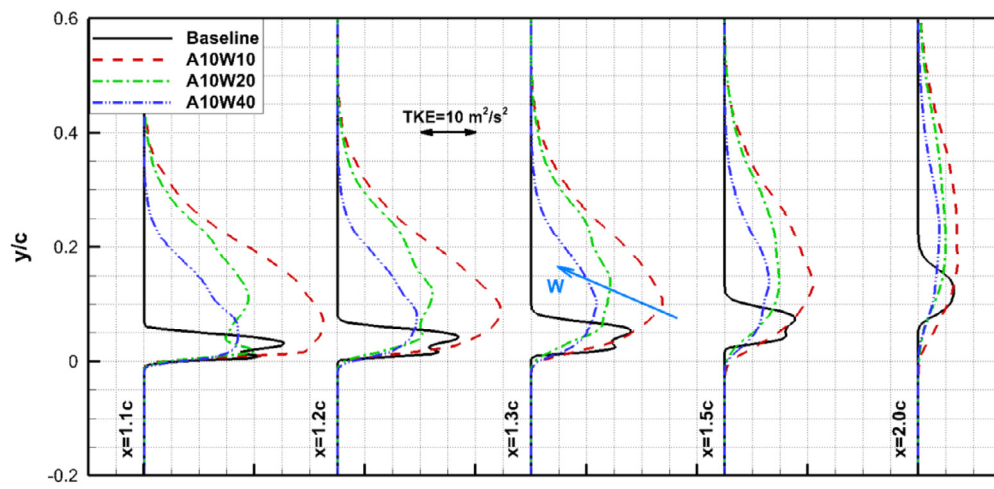
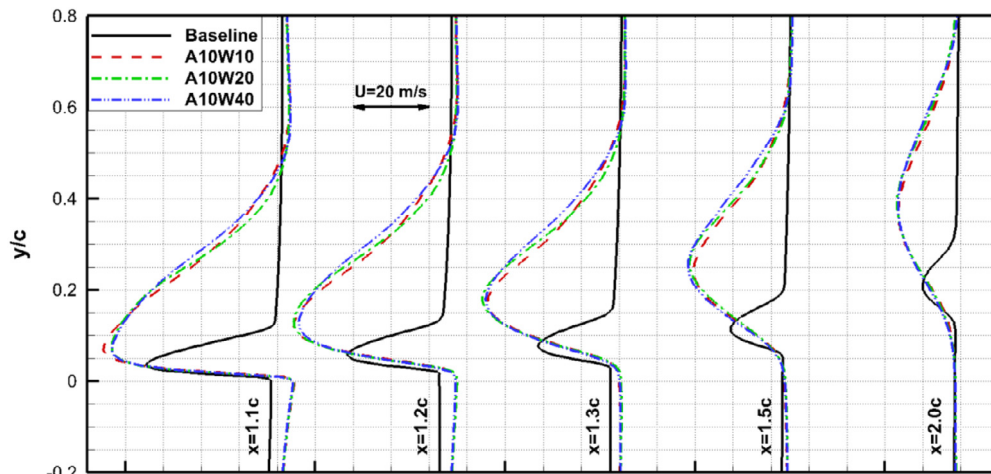


**Fig. 17.** Effect of wavelength: wake development at AOA = 10°.

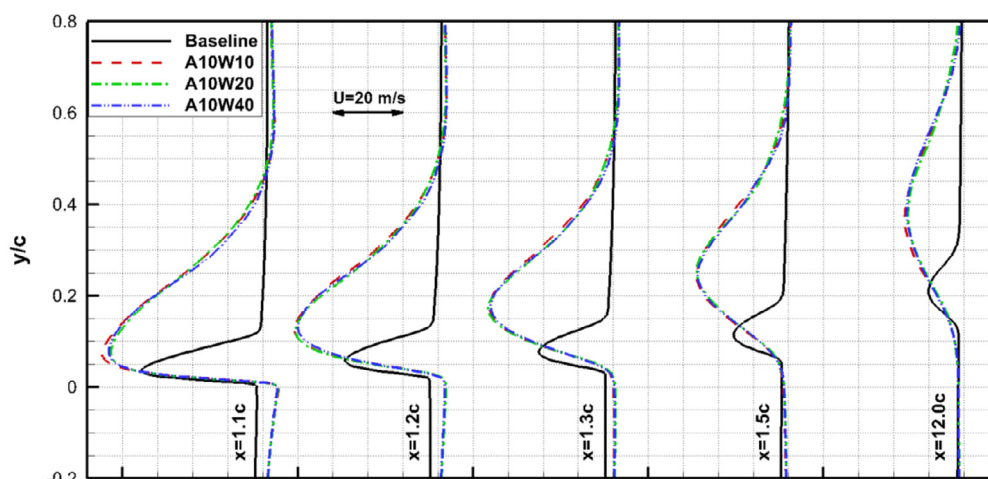


(d) TKE at trough position

Fig. 17. (continued)

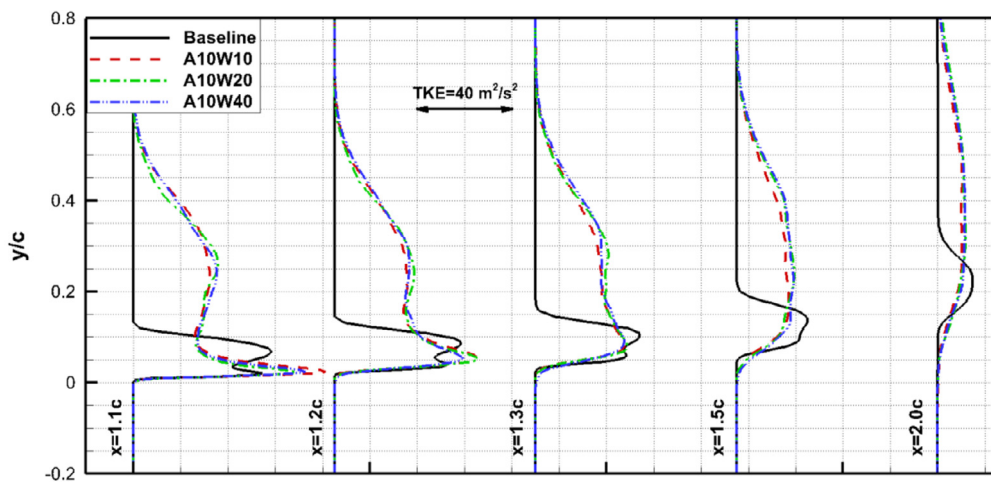


(a) Mean velocity at peak position

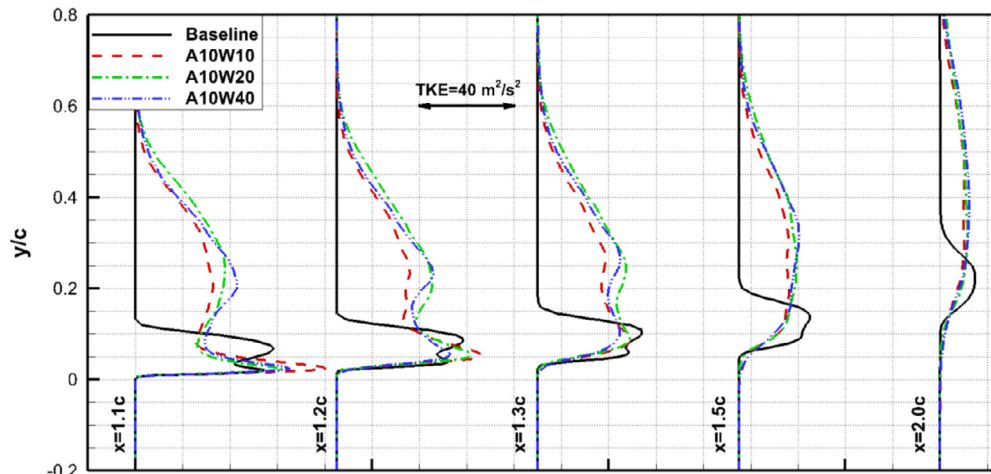


(b) Mean velocity at trough position

Fig. 18. Effect of wavelength: wake development at AOA = 15°.

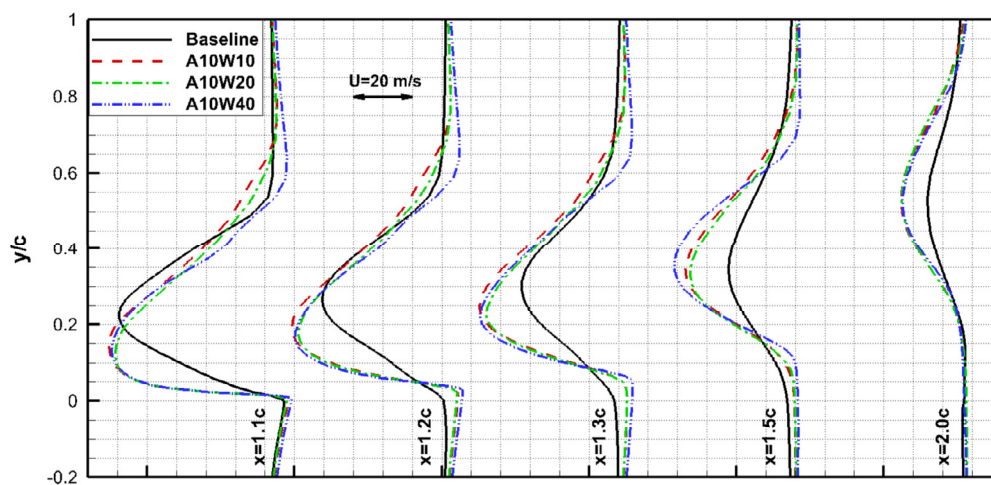


(c) TKE at peak position



(d) TKE at trough position

Fig. 18. (continued)



(a) Mean velocity at peak position

Fig. 19. Effect of wavelength: wake development at AOA = 20°.

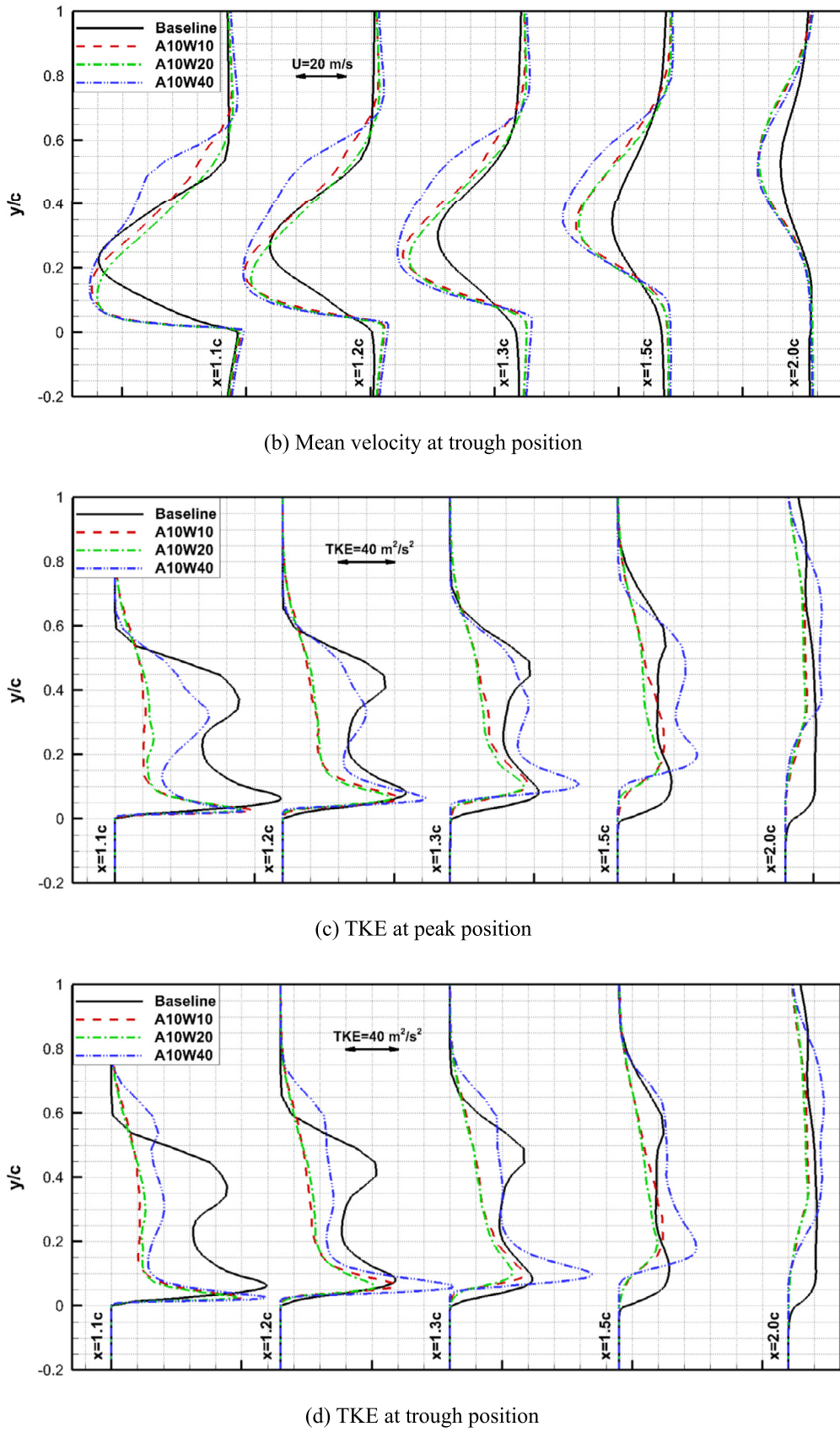
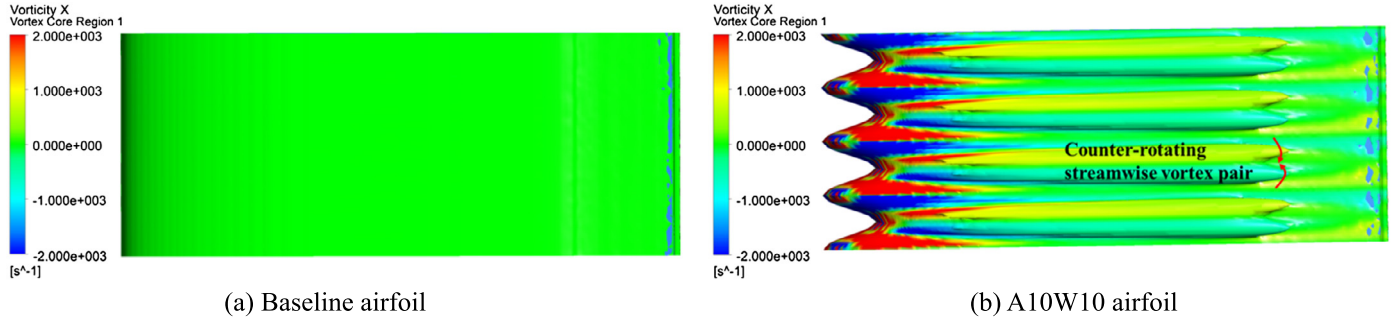
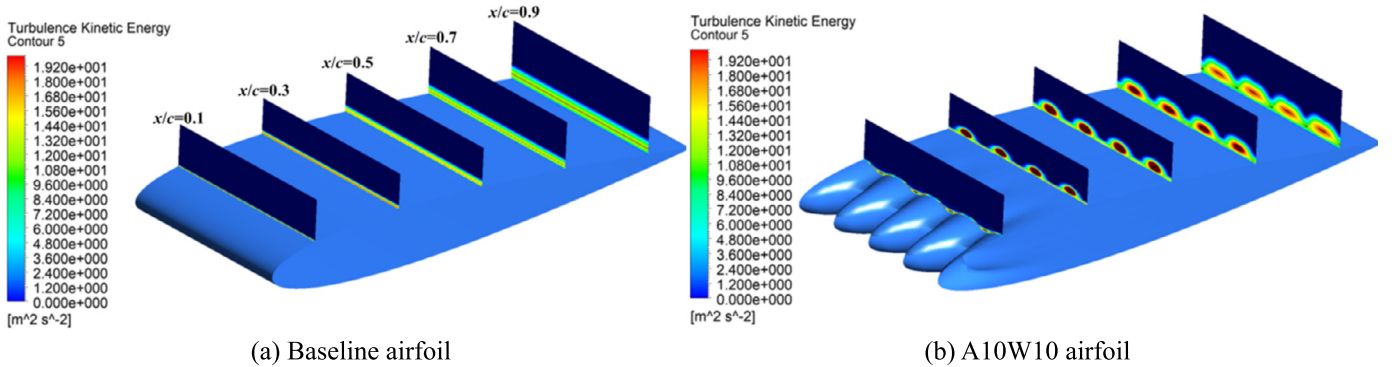


Fig. 19. (continued)



**Fig. 20.** Vortex structures distributions on the suction side at an angle of attack of 5° ( $Q = 50000 \text{ s}^{-2}$ ). (For interpretation of the colors in the figure(s), the reader is referred to the web version of this article.)



**Fig. 21.** TKE distributions on the suction side at an angle of attack of 5°.

#### 4.3. Flow structures

The second invariant property of the velocity gradient ( $Q$ -criterion) is defined by

$$Q = \frac{1}{2} (\Omega_{ij}\Omega_{ji} - S_{ij}S_{ji}) \quad (8)$$

where  $\Omega_{ij} = \partial u_i / \partial x_j - \partial u_j / \partial x_i$  and  $S_{ij} = \partial u_i / \partial x_j + \partial u_j / \partial x_i$  are the rotation tensor and strain rate tensor, respectively. The iso-surface of the  $Q$ -criterion colored by the streamwise vorticity is plotted in Fig. 20 for the baseline and A10W10 airfoils at an angle of attack of 5°. Very distinct flow patterns are observed between the baseline and wavy airfoils. The flow topologies are uniform in the spanwise for the baseline airfoil, while periodic distributions of flow structures are observed for the wavy airfoil. There is a thin vortex sheet in the boundary layer of the baseline airfoil, while a pair of counter-rotating streamwise vortices is generated behind each trough of the wavy airfoil. These induced streamwise vortices enhance the momentum exchange and turbulent fluctuations in the downstream boundary layer, as can be seen from Fig. 21.

Fig. 22 shows the instantaneous three-dimensional coherent vortex structures at large angles of attack of 17° and 20° for the baseline and A10W10 airfoils. The iso-surface of the  $Q$ -criterion is colored by the Mach number in this figure. A typical leading edge separation is found for the baseline airfoil and a large-scale coherent spanwise vortex rolls up from the leading edge of the airfoil. The periodic vortex shedding causes a periodic variation of the lift and drag coefficients, as shown in Fig. 9. The flow patterns of the wavy airfoil are obviously different from those of the baseline airfoil. Complicated small-scale vortices are observed for the wavy airfoil. These characteristics mean that the WLEs can break down the large-scale vortex into small-scale vortices, which is believed to be beneficial for noise control [34,35].

The distributions of the instantaneous spanwise vorticity at an angle of attack of 20° are shown in Fig. 23 for the baseline and A10W0 airfoils. Three spanwise positions corresponding to the peak, middle and trough are shown for the wavy airfoil. Large-scale coherent vortex structures shed from both the leading edge and trailing edge of the baseline airfoil and the two vortex structures rotate in the opposite directions, as shown in Fig. 23(a). The flow patterns of the wavy airfoil are quite different from the baseline airfoil. The large-scale vortex structures are broken down into small-scale vortices.

#### 5. Conclusions

The objective of the present study is to investigate the effect of the WLEs on the airfoil aerodynamic performance and wake development. Numerical simulations are carried out to study the flow patterns around the airfoils with various angles of attack at a Reynolds number of 400 000. Five wavy airfoils with different amplitudes and wavelengths and one baseline airfoil with a straight leading edge are simulated.

In the pre-stall region of the baseline airfoil, the numerical results show that the lift curve slope, the maximum lift coefficient and the maximum lift-to-drag ratio are reduced by the wavy airfoil. Moreover, the aerodynamic performance of the wavy airfoil is sensitive to both the amplitude and wavelength. The WLE with the largest amplitude and smallest wavelength generally result in the worst aerodynamic performance in terms of the above parameters. For example, the maximum lift coefficient is reduced from 1.29 to 0.79 and the maximum lift-to-drag ratio is reduced from 37.4 to 24.4 by the wavy A10W10 airfoil with the largest amplitude and smallest wavelength. However, in the post-stall regime of the baseline airfoil, the drag coefficient is decreased significantly by the WLEs and the lift-to-drag ratios of the wavy airfoils are al-

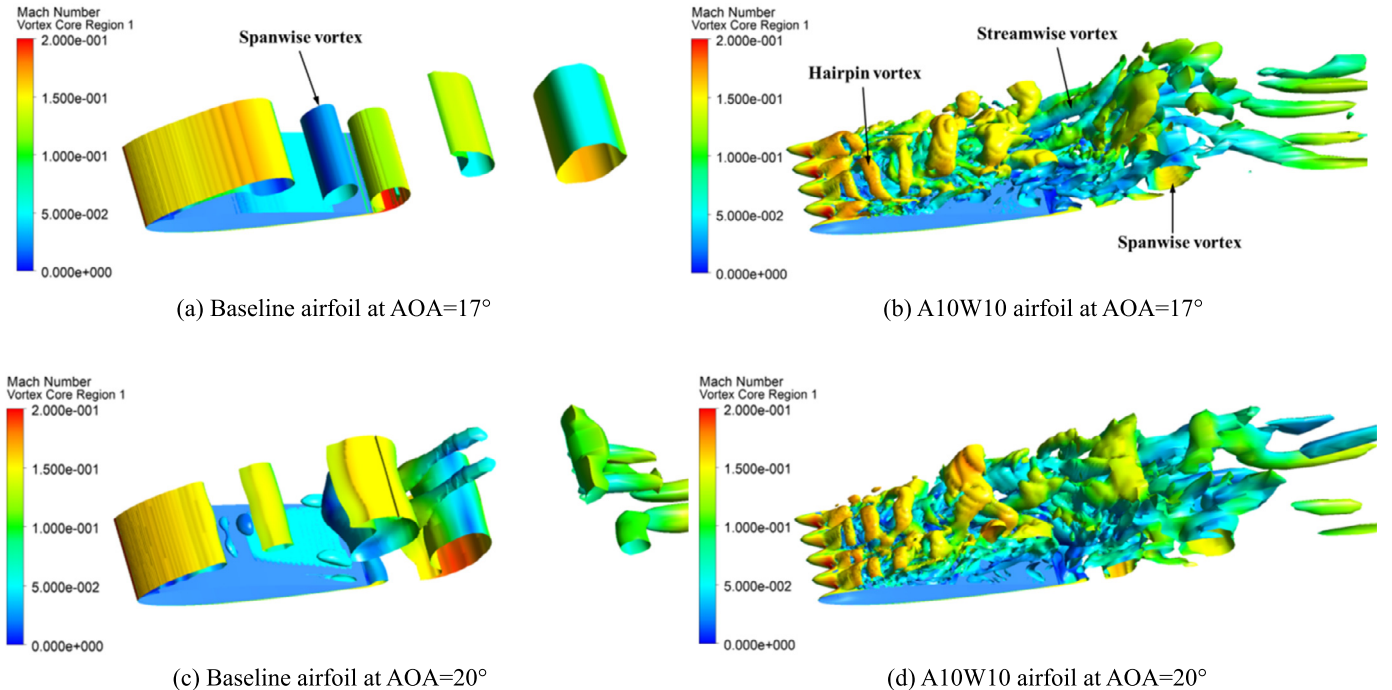


**Fig. 22.** Three-dimensional vortex structures distributions at large angles of attack ( $Q = 500000 \text{ s}^{-2}$ ).

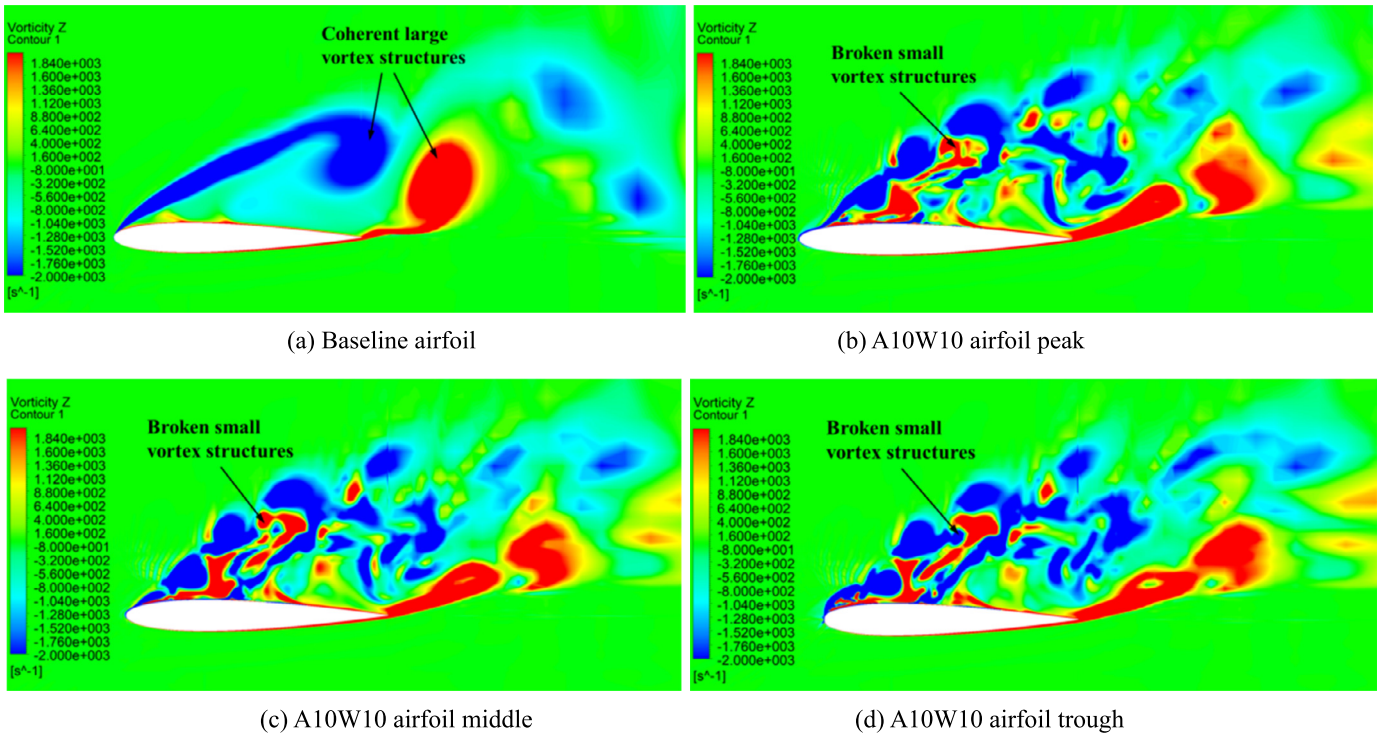


**Fig. 23.** Instantaneous spanwise vorticity distributions at an angle of attack of 20°.

most consistent with those of the baseline airfoil. In addition, the wavy airfoils exhibit a soft stall process with no abrupt decrease of the lift when the wavy amplitude is large enough. The lift and drag fluctuations are also reduced by the wavy airfoil in the post-stall regime, which is believed to be beneficial for airfoil separation-stall noise reduction.

The wake velocity and TKE profiles are altered a lot by the wavy airfoils. At small angles of attack, higher wake deficit and TKE are

observed for the wavy airfoil at the trough position, while lower values can be achieved at the peak position. At large angles of attack, higher wake deficit is found at both the peak and trough positions. However, the TKE in the wake could be reduced significantly by the wavy airfoil in the post-stall regime. In general, the wake is shifted slightly towards the suction side by the wavy modification in the pre-stall regime, while it is shifted towards the pressure side in the post-stall regime.

## Declaration of competing interest

The authors declare that they have no known competing financial interests or personal relationships that could have appeared to influence the work reported in this paper.

## Acknowledgement

This work is supported by the National Natural Science Foundation of China (grant numbers 51776174, 51936010) and the National Science and Technology Major Project of China (grant number 2017-II-0008-0022).

## References

- [1] Y.X. Luo, F.B. Wen, S. Wang, S.B. Zhang, S.T. Wang, Z.Q. Wang, Numerical investigation on the biomimetic trailing edge of a high-subsonic turbine blade, *Aerosp. Sci. Technol.* 89 (2019) 230–241.
- [2] X.C. Mao, B. Liu, B.T. Zhang, Hub clearance effects of a cantilevered tandem stator on the performance and flow behaviors in a small-scale axial flow compressor, *Aerosp. Sci. Technol.* 91 (2019) 219–230.
- [3] R.F. Yang, D.D. Zhong, N. Ge, Numerical investigation on flow control effects of dynamic hump for turbine cascade at different Reynolds number and hump oscillating frequency, *Aerosp. Sci. Technol.* 92 (2019) 280–288.
- [4] S.H. Kim, K.Y. Kim, Effects of installation location of fluidic oscillators on aerodynamic performance of an airfoil, *Aerosp. Sci. Technol.* 99 (2020).
- [5] F.E. Fish, J.M. Battle, Hydrodynamic design of the humpback whale flipper, *J. Morphol.* 225 (1995) 51–60.
- [6] D.S. Miklosovic, M.M. Murray, L.E. Howle, F.E. Fish, Leading-edge tubercles delay stall on humpback whale (*Megaptera novaeangliae*) flippers, *Phys. Fluids* 16 (5) (2004) 39–42.
- [7] D.S. Miklosovic, M.M. Murray, L.E. Howle, Experimental evaluation of sinusoidal leading edges, *J. Aircr.* 44 (4) (2007) 1404–1407.
- [8] H. Johari, C. Henoch, D. Custodio, A. Levshin, Effects of leading-edge protuberances on airfoil performance, *AIAA J.* 45 (11) (2007) 2634–2642.
- [9] K.L. Hansen, R.M. Kelso, B.B. Dally, Performance variations of leading-edge tubercles for distinct airfoil profiles, *AIAA J.* 49 (1) (2011) 185–194.
- [10] J. Guerreiro, J. Sousa, Low-Reynolds-number effects in passive stall control using sinusoidal leading edges, *AIAA J.* 50 (2) (2012) 461–469.
- [11] M.M. Zhang, G.F. Wang, J.Z. Xu, Aerodynamic control of low-Reynolds-number airfoil with leading-edge protuberances, *AIAA J.* 51 (8) (2013) 1960–1971.
- [12] M. Bolzon, R.M. Kelso, M. Arjomandi, Formation of vortices on a tubercled wing, and their effects on drag, *Aerosp. Sci. Technol.* 56 (2016) 46–55.
- [13] M.C. Keerthi, M.S. Rajeshwaran, A. Kushari, A. De, Effect of leading-edge tubercles on compressor cascade performance, *AIAA J.* 54 (3) (2016) 912–923.
- [14] K.L. Hansen, N. Rostamzadeh, R.M. Kelso, B.B. Dally, Evolution of the streamwise vortices generated between leading edge tubercles, *J. Fluid Mech.* 788 (2016) 730–766.
- [15] M. Bolzon, R.M. Kelso, M. Arjomandi, Force measurements and wake surveys of a swept tubercled wing, *J. Aerosp. Eng.* 30 (3) (2017) 1–11.
- [16] S. Sudhakar, N. Karthikeyan, L. Venkatakrishnan, Influence of leading edge tubercles on aerodynamic characteristics of a high aspect-ratio UAV, *Aerosp. Sci. Technol.* 69 (2017) 281–289.
- [17] C. Cai, Z.G. Zuo, T. Maeda, Y. Kamada, Q.A. Li, K. Shimamoto, S. Liu, Periodic and aperiodic flow patterns around an airfoil with leading-edge protuberances, *Phys. Fluids* 29 (2017) 115110.
- [18] Z.Y. Wei, T.H. New, Y.D. Cui, An experimental study on flow separation control of hydrofoils with leading-edge tubercles at low Reynolds number, *Ocean Eng.* 108 (2015) 336–349.
- [19] Z.Y. Wei, B. Zang, T.H. New, Y.D. Cui, A proper orthogonal decomposition study on the unsteady flow behaviour of a hydrofoil with leading-edge tubercles, *Ocean Eng.* 121 (2016) 356–368.
- [20] Z.Y. Wei, T.H. New, Y.D. Cui, Aerodynamic performance and surface flow structures of leading-edge tubercled tapered swept-back wings, *AIAA J.* 56 (1) (2018) 423–431.
- [21] Z.Y. Wei, L. Lian, Y.S. Zhong, Enhancing the hydrodynamic performance of a tapered swept-back wing through leading-edge tubercles, *Exp. Fluids* 59 (2018) 1–10.
- [22] Z.Y. Wei, T.H. New, L. Lian, Y.N. Zhang, Leading-edge tubercles delay flow separation for a tapered swept-back wing at very low Reynolds number, *Ocean Eng.* 181 (2019) 173–184.
- [23] Z.Y. Wei, J.W.A. Toh, I.H. Ibrahim, Y.N. Zhang, Aerodynamic characteristics and surface flow structures of moderate aspect-ratio leading-edge tubercled wings, *Eur. J. Mech. B, Fluids* 75 (2019) 143–152.
- [24] P.W. Weber, L.E. Howle, M.M. Murray, D.S. Miklosovic, Computational evaluation of the performance of lifting surfaces with leading-edge protuberances, *J. Aircr.* 48 (2) (2011) 591–600.
- [25] H.S. Yoon, P.A. Hung, J.H. Jung, M.C. Kim, Effect of the wavy leading edge on hydrodynamic characteristics for flow around low aspect ratio wing, *Comput. Fluids* 49 (2011) 276–289.
- [26] A.K. Malipeddi, N. Mahmoudnejad, K. Hoffmann, Numerical analysis of effects of leading-edge protuberances on aircraft wing performance, *J. Aircr.* 49 (5) (2012) 1336–1344.
- [27] Y.F. Lin, K. Lam, L. Zou, Y. Liu, Numerical study of flows past airfoils with wavy surfaces, *J. Fluid Struct.* 36 (2013) 136–148.
- [28] A. Skilen, A. Revell, A. Pinelli, U. Piomelli, J. Favier, Flow over a wing with leading-edge undulations, *AIAA J.* 53 (2) (2015) 464–472.
- [29] R.P. Torro, J.W. Kim, A large-eddy simulation on a deep-stalled aerofoil with a wavy leading edge, *J. Fluid Mech.* 813 (2017) 23–52.
- [30] M. Zhao, Y.J. Zhao, Z.X. Liu, Dynamic mode decomposition analysis of flow characteristics of an airfoil with leading edge protuberances, *Aerosp. Sci. Technol.* 98 (2020).
- [31] E. Nierop, S. Alben, M.P. Brenner, How bumps on whale flippers delay stall: an aerodynamic model, *Phys. Rev. Lett.* 100 (2008) 1–4.
- [32] N. Rostamzadeh, R.M. Kelso, B.B. Dally, K.L. Hansen, The effect of undulating leading-edge modifications on NACA0021 airfoil characteristics, *Phys. Fluids* 25 (2013) 1–19.
- [33] K.L. Hansen, R.M. Kelso, C.J. Doolan, Reduction of flow induced tonal noise through leading edge tubercle modifications, *AIAA 2010-3700*, 2010.
- [34] G. Lacagnina, S.M. Hasheminejad, P. Chaitanya, P. Joseph, T.P. Chong, O. Stalnov, Leading edge serrations for the reduction of aerofoil separation self-noise, *AIAA 2017-4169*, 2017.
- [35] G. Lacagnina, P. Chaitanya, T. Berk, P. Joseph, S.M. Hasheminejad, O. Stalnov, T.P. Chong, B. Ganapathisubramani, Effect of leading edge serrations in reducing aerofoil noise near stall conditions, *AIAA 2018-3285*, 2018.
- [36] M. Zhang, A. Frendi, Effect of airfoil leading edge waviness on flow structures and noise, *Int. J. Numer. Methods Heat Fluid Flow* 26 (6) (2016) 1821–1842.
- [37] J.W. Kim, S. Haeri, P.F. Joseph, On the reduction of aerofoil-turbulence interaction noise associated with wavy leading edges, *J. Fluid Mech.* 792 (2016) 526–552.
- [38] J.M. Turner, J.W. Kim, On the universal trends in the noise reduction due to wavy leading edges in aerofoil-vortex interaction, *J. Fluid Mech.* 871 (2019) 186–211.
- [39] W.J. Chen, W.Y. Qiao, F. Tong, L.F. Wang, X.N. Wang, Experimental investigation of wavy leading edges on rod-aerofoil interaction noise, *J. Sound Vib.* 422 (2018) 409–431.
- [40] W.J. Chen, W.Y. Qiao, F. Tong, L.F. Wang, X.N. Wang, Numerical investigation of wavy leading edges on rod-airfoil interaction noise 56 (7) (2018) 2553–2567.
- [41] F. Tong, W.Y. Qiao, K.B. Xu, L.F. Wang, W.J. Chen, X.N. Wang, On the study of wavy leading-edge vanes to achieve low fan interaction noise, *J. Sound Vib.* 419 (2018) 200–226.
- [42] ANSYS, ANSYS CFX-Solver Theory Guide, Release 14.0, ANSYS Inc., Pennsylvania, 2014.
- [43] F.R. Menter, Two-equation eddy-viscosity turbulence models for engineering applications, *AIAA J.* 32 (8) (1994) 1598–1605.
- [44] F.R. Menter, Y. Egordov, The scale-adaptive simulation method for unsteady turbulent flow predictions. Part 1: theory and model description, *Flow Turbul. Combust.* 85 (2010) 113–138.
- [45] Y. Egordov, F.R. Menter, R. Lechner, D. Cokljat, The scale-adaptive simulation method for unsteady turbulent flow predictions, Part 2: application to complex flows, *Flow Turbul. Combust.* 85 (2010) 139–165.
- [46] B.M. Duda, F.R. Menter, S. Deck, H. Bezahl, T. Hansen, M.J. Esteve, Application of the scale-adaptive simulation to a hot jet in cross flow, *AIAA J.* 51 (3) (2013) 674–685.
- [47] S. Maleki, D. Burton, M.C. Thompson, Assessment of various turbulence models (ELES, SAS, URANS and RANS) for predicting the aerodynamics of freight train container wagons, *J. Wind Eng. Ind. Aerodyn.* 170 (2017) 68–80.
- [48] G.J.M. Loupy, G.N. Barakos, N.J. Taylor, Store release trajectory variability from weapon bays using scale-adaptive simulations, *AIAA J.* 56 (2) (2018) 752–764.
- [49] A. Rezaieha, H. Montazeri, B. Blocken, CFD analysis of dynamic stall on vertical axis wind turbines using scale-adaptive simulation (SAS): comparison against URANS and hybrid RANS/LES, *Energy Convers. Manag.* 196 (2019) 1282–1298.
- [50] C.Y. Xu, T. Zhang, Y.Y. Yu, J.H. Sun, Effect of von Karman length scale in scale adaptive simulation approach on the prediction of supersonic turbulent flow, *Aerosp. Sci. Technol.* 86 (2019) 630–639.
- [51] C.L. Ladson, Effects of independent variation of Mach and Reynolds numbers on the low-speed aerodynamic characteristics of the NACA0012 airfoil section, NASA Technical Memorandum, 1988-4074, 1988.
- [52] X. Liu, M. Azarpeyvand, R. Theunissen, On the aerodynamic performance of serrated airfoils, in: The 22nd International Congress on Sound and Vibration, 2015.
- [53] P.F. Zhang, A.B. Liu, J.J. Wang, Aerodynamic modification of a NACA 0012 airfoil by trailing-edge plasma Gurney flap, *AIAA J.* 47 (10) (2009) 2467–2474.
- [54] T.S. Liu, J. Montefort, W. Liou, S.R. Pantula, Q.A. Shams, Lift enhancement by static extended trailing edge, *J. Aircr.* 44 (6) (2007) 1939–1947.

- [55] M. Drela, M.B. Giles, Viscous-inviscid analysis of transonic and low Reynolds number airfoil, *AIAA J.* 25 (10) (1987) 1347–1355.
- [56] J.D. Anderson, *Fundamentals of Aerodynamics*, sixth edition, McGraw-Hill Education, 2016.
- [57] J.C. Date, S.R. Turnock, Computational evaluation of the periodic performance of a NACA 0012 fitted with a Gurney flap, *J. Fluids Eng.* 124 (2002) 227–234.
- [58] D.R.M. Jeffrey, An investigation into the aerodynamics of Gurney flaps, Ph.D thesis, University of Southampton, 1998.
- [59] E. Berton, C. Allain, D. Favier, C. Maresca, Experimental methods for subsonic flow measurements, *Notes Numer. Fluid Mech. Multidiscipl. Des.* 81 (2002) 97–104.
- [60] R. Bourguet, M. Braza, G. Harran, R. Akoury, Anisotropic organised eddy simulation for the prediction of non-equilibrium turbulent flows around bodies, *J. Fluids Struct.* 24 (2008) 1240–1251.